ORIGINAL RESEARCH Open access

Cooperative Transport of Cable-Suspended Payloads Using Two Quadrotors with Y-Shaped Suspension

Gabriel Costa[1*], Lucas Ribeiro[1], Ricardo Alves[2], Mariana Lopes[3], Felipe Rocha[4]

Abstract

This article presents an original “Y”-configured tether arrangement for cooperative transport of a load by a pair of quadrotors, streamlining both load attachment and release. Compared with the established “V”-form rigging, the new configuration introduces an additional oscillatory axis into the combined quadrotor–load dynamics, thereby making the system formulation and regulation substantially more intricate. The modeling procedure separates the suspended object’s motion into two orthogonal planes—longitudinal and lateral sway—and embeds the resulting oscillatory effects into the two vehicles’ dynamics as perturbing tensile forces exerted by the cables. A new navigation and regulation architecture is established, consisting of a guidance law engineered to enable formation reconfiguration while simultaneously providing a local path reference to any quadrotor lacking the global plan. On this basis, a cooperative regulation strategy is constructed by incorporating an uncertainty and disturbance estimator to actively neutralize swing-induced perturbations, thereby achieving the prescribed formation-tracking behavior. An investigation grounded in singular perturbation theory confirms that a proposed parameter unification scheme—which consolidates tuning across multiple control loops—enables a single coefficient, ε, to improve both formation precision and disturbance immunity equivalently. Numerical experiments across diverse scenarios validate the technique’s strength.

Keywords Cooperative aerial transportation, Suspended payload swing modeling, Guidance law, Cooperative formation control, Disturbance rejection

*Correspondence:
Gabriel Costa
gabriel.costa@ufmg.br
[1] Department of AI for Coffee Cherry and Bean Quality Grading, Faculty of Agriculture, Federal University of Minas Gerais, Belo Horizonte, Brazil
[2] Department of Machine Learning for Harvest Scheduling Optimization, Faculty of Agriculture, University of Coimbra, Coimbra, Portugal
[3] Department of Smart Post-Harvest Drying Analytics, Faculty of Agriculture, University of São Paulo, São Paulo, Brazil
[4] Department of Precision Crop Rotation Planning, Faculty of Agriculture, Federal University of Rio Grande do Sul, Porto Alegre, Brazil

Introduction

The utilization of rotorcraft for the carriage of cable-dangled objects represents a vital theme in operational contexts. The existing literature is predominantly concerned with single-vehicle transportation [1-3], emphasizing the suppression of load vibration and aircraft stabilization. Single-vehicle configurations, nonetheless, are constrained by intrinsically limited lifting performance, vulnerability, and an absence of load orientation functionality. These deficiencies have, in recent times, drawn scholarly attention to collaborative multi-vehicle transport as a remedy.

To narrow the scope, the cooperative system examined here couples two quadrotors to a single load via suspension cables. Deploying such a configuration in practice poses several difficulties. A primary difficulty is the mechanism for depositing the load at the designated point. As illustrated in **Figure 1**, existing studies classify rigging topologies into two

This is an open access article distributed under the terms of the Creative Commons Attribution-NonCommercial-ShareAlike 4.0 International License (CC BY-NC-SA 4.0), which permits non-commercial use, distribution, reproduction, and adaptation in any medium or format, provided that appropriate credit is given to the original author(s) and source, a link to the license is provided, and any changes made are indicated. Adapted material must be distributed under the same license.

© 2023 The Author(s). | Published by Agro Intelligence Research Press

variants: the “V” configuration [4-6] and the trapezoidal configuration [7-9]. Disengaging the load under either method requires a pair of decoupling units, either fitted to the aircraft or to the object.

In contrast, this work advances an innovative “Y” topology that relies on a single automated decoupling unit positioned on the cable itself. Beyond the obvious cost-saving aspect, the proposed arrangement halves both the time and the manual effort required to secure the load. A further advantage of using a single release unit is the elimination of the load-tilting phenomenon that arises when two decouplers actuate out of sync—a practically meaningful attribute in scenarios such as parcel dropping. Against the backdrop of “V”-form rigging, the proposed topology adds an extra swinging axis, making the task of formation regulation notably harder.

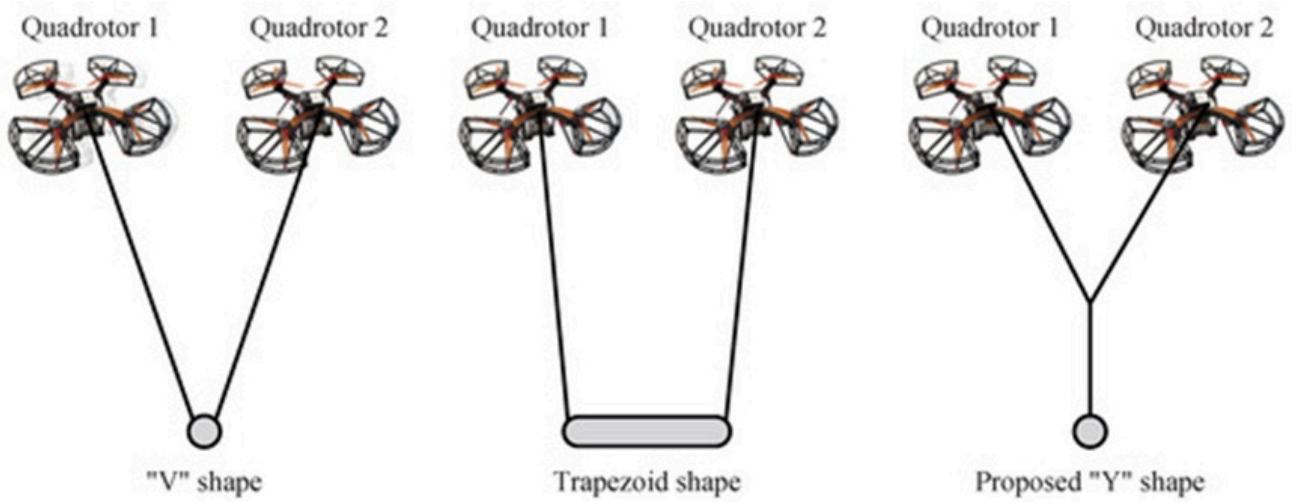

Figure 1. A comparison among the “V”-shaped [4-6], trapezoid-shaped [7-9], and the proposed “Y”-shaped suspension method.

The orchestration of dual-quadrotor formation flight represents a second major obstacle. Prevailing strategies can be divided into those anchored in a virtual-leader framework and those in a leader–follower arrangement, the latter assigning one aircraft to trail another at a prescribed offset. Synergy under either framework is achieved by feeding a global reference, along with neighbor data obtained via a communication link, into each local controller. However, the specific nature of the exchanged data varies. In Ccari and Yanyachi [10], the load’s designated trajectory is treated as an intangible leader, with the two vehicles tracking this trajectory while preserving formation. Taking a different approach, Aliyu and El Ferik [11] propose a neural network-based graph-theoretic distributed adaptive method; here, a global heading reference is broadcast to maintain path geometry in leader–follower mode.

In contrast to Aliyu and El Ferik [11], who each quadrotor receives global references, Chen and Shan [12] stipulate that only the lead aircraft is privy to the global objective. At the same time, the second utilizes a PID-type regulator to shadow the lead at a fixed spacing. This method, however, restricts flight to the x-direction. Collectively, these observations reveal that achieving collaborative path-following ordinarily presumes full global path awareness at both vehicles; when such awareness is partial, the achievable formation maneuvers become severely curtailed. Hence, the question of harnessing incomplete global path data for sophisticated formation behaviors—encompassing path tracking and geometric reconfiguration—remains open.

A third difficulty is achieving stable, high-precision path adherence in the presence of tensile perturbations induced by a swaying suspended load, which compounds the system’s underactuation and degrees of freedom [13] and degrades its robustness. Chai *et al.* [14] proposed an energy-based, nonlinear, adaptive law to stabilize the closed-loop dynamics under sway conditions. Still, robustness levels cannot be tuned in a straightforward quantitative manner. Lin *et al.* [15] present a reinforcement learning-driven position regulator for accurate delivery and stabilization, shown in simulation to

© 2023 The Author(s). | Published by Agro Intelligence Research Press

reject uncertain disturbances, sway included. Adoption of this method presupposes a training phase, and there exists no rigorous mathematical guarantee for the resulting stability and resilience. To handle loads of varying mass, Villa *et al.* [7] introduce an adaptive dynamic compensator-based cooperative controller for online estimation of parameter variations caused by mass changes. The authors caution, however, that the framework performs as intended only when the system moves at near-constant speed along a path with limited acceleration. In Ccari and Yanyachi [10], the authors construct a sliding mode formation regulator paired with a nonlinear disturbance observer to estimate and compensate external forces and sway. However, this is accompanied by undesirable chattering in the actuation signal. The collective effort notwithstanding, the design of a compact yet high-performance cooperative regulator capable of delivering quantitatively specifiable robustness against sway-induced perturbations remains an unresolved objective.

To address all three challenges outlined, this paper proposes a methodical solution to the cooperative carriage problem that features the novel “Y”-form rigging. To capture the physical essence of this aircraft–load system, a sway model is first developed by partitioning the motion into a forward–backward plane and a lateral plane, then expressing the swing as tensile perturbation forces that feed into the dynamics of each quadrotor. The resulting composite model is strongly coupled and nonlinear; accordingly, feedback linearization is applied to decompose the system into six channels, each of which matches the template of a perturbed second-order process. A guidance rule is crafted for the two aircraft to reach the required formation and adapt its shape, and—critically—for the quadrotor lacking the global path, the rule constructs a local reference derived from its neighbor’s condition and command input. In addition to this rule, a robust cooperative regulation strategy is implemented, using an uncertainty and disturbance estimator (UDE) to evaluate and cancel external forces and sway disturbances in an online fashion. To attain the commanded disturbance suppression and tracking specification, a mapping scheme is introduced for the UDE that compresses the tuning of all channels into a single parameter, ε. A singular-perturbation-based analysis validates this mapping, demonstrating that monotonically decreasing ε bolsters the system’s robustness and path-following correctness in a quantifiable way. Numerical simulation results demonstrate the high performance of the proposed guidance and robust regulation framework across several flight scenarios. The article’s advances are itemized as follows:

· We propose a novel “Y”-shaped suspension method to improve payload carrying and dropping efficiency, and a payload swing model is derived specifically for the “Y”-shaped suspension to show explicitly how swing disturbance affects the motion of the quadrotors.

· A novel, comprehensive design of the guidance law and UDE-based cooperative control is proposed for the “Y”-shaped quadrotor–payload system to achieve not only robust formation control but also high-accuracy trajectory tracking under the communication constraint of only one quadrotor having access to the global trajectory reference. Moreover, the proposed guidance law features capabilities for formation transformation and flight mode variation to enable complex flight maneuvers, such as cooperative obstacle avoidance in a cluttered environment.

· In contrast to the frequency-domain analysis [16], this paper provides a rigorous time-domain-based stability and robustness analysis using singular perturbation theory. It proposes a parameter-mapping method to unify parameter tuning across different control channels. The analysis shows that the formation trajectory tracking accuracy and robustness against payload swing disturbances are monotonically related to a single designable parameter, ε, enabling system performance to be easily and quantitatively improved.

The rest of this paper is organized as follows: In Section 2, dynamic and kinematic models of the quadrotors and the suspended payload are derived, and then simplified for control design. Section 3 presents the design of the guidance law and the UDE-based cooperative controller, followed by the stability and performance analysis of the closed-loop system. In Section 4, simulation results demonstrate the effectiveness of the proposed approach across different scenarios. Finally, conclusions are drawn in Section 5.

Problem Formation

© 2023 The Author(s). | Published by Agro Intelligence Research Press

Tables 1 and 2 compile the notation and physical quantities that characterize the quadrotor–payload ensemble. Within these tables, a superscript drawn from $\{\mathcal{I}, \mathcal{B}, \mathcal{L}\}$ signals the coordinate frame in which a given quantity is resolved, and the subscript $i \in \{1,2\}$ serves to distinguish between the two aircraft.

Table 1. Quadrotor–payload system variable definitions.

Symbols	Variable description
$\boldsymbol{P}_i^{\mathcal{I}} = \left[x_i^{\mathcal{I}},\ y_i^{\mathcal{I}},\ z_i^{\mathcal{I}}\right]^T$	Position of the i-th quadrotor
$\boldsymbol{P}_p^{\mathcal{I}} = \left[x_p^{\mathcal{I}},\ y_p^{\mathcal{I}},\ z_p^{\mathcal{I}}\right]^T$	Position of the payload
$\phi i, \theta i, \psi i$	Rotation angles of the i-th quadrotor
$\boldsymbol{V}_i^{\mathcal{B}} = \left[V_{ix}^{\mathcal{B}},\ V_{iy}^{\mathcal{B}},\ V_{iz}^{\mathcal{B}}\right]^T$	Linear velocity of the i-th quadrotor
$\boldsymbol{V}_p^{\mathcal{I}} = \left[V_{px}^{\mathcal{I}},\ V_{py}^{\mathcal{I}},\ V_{pz}^{\mathcal{I}}\right]^T$	Linear velocity of the payload
$\boldsymbol{\omega}_i^{\mathcal{B}} = \left[\omega_{ix}^{\mathcal{B}},\ \omega_{iy}^{\mathcal{B}},\ \omega_{iz}^{\mathcal{B}}\right]^T$	Angular velocity of the i-th quadrotor
$\omega ia, \omega ib, \omega ic, \omega id$	Rotor rotation speeds of the i-th quadrotor
$\Omega i = -\omega ia - \omega ib + \omega ic + \omega id$	Sum of the rotor rotation speeds of the i-th quadrotor
$F_{iqz}^{\mathcal{B}}$	Thrust command for the i-th quadrotor
$\boldsymbol{\tau}_i^{\mathcal{B}} = \left[\tau_{ix}^{\mathcal{B}},\ \tau_{iy}^{\mathcal{B}},\ \tau_{iz}^{\mathcal{B}}\right]^T$	Torque command for the i-th quadrotor
$\boldsymbol{F}_{iaq}^{\mathcal{B}} = \left[F_{iaqx}^{\mathcal{B}},\ F_{iaqy}^{\mathcal{B}},\ F_{iaqz}^{\mathcal{B}}\right]^T$	Air drag on the i-th quadrotor
$\boldsymbol{F}_{Dp}^{\mathcal{I}} = \left[F_{Dpx}^{\mathcal{I}},\ F_{Dpy}^{\mathcal{I}},\ F_{Dpz}^{\mathcal{I}}\right]^T$	Air drag on the payload
$\boldsymbol{T}_p^{\mathcal{I}} = \left[T_{px}^{\mathcal{I}},\ T_{py}^{\mathcal{I}},\ T_{pz}^{\mathcal{I}}\right]^T$	Cable pulling force on the payload

© 2023 The Author(s). | Published by Agro Intelligence Research Press

$\boldsymbol{T}_i^{\mathcal{I}} = \left[T_{ix}^{\mathcal{I}},\ T_{iy}^{\mathcal{I}},\ T_{iz}^{\mathcal{I}}\right]^T$	Cable pulling force on the i-th quadrotor
$\boldsymbol{F}_{iDq}^{\mathcal{B}} = \left[F_{iDqx}^{\mathcal{B}},\ F_{iDqy}^{\mathcal{B}},\ F_{iDqz}^{\mathcal{B}}\right]^T$	Total disturbance force on the i-th quadrotor
α, β	Payload swing angles
δ	Quadrotor formation yaw angle
λ	The angle between the cables that connect the quadrotors
L	Formation size: the distance between the two quadrotors
$\boldsymbol{A}_{\alpha}^{\mathcal{I}} = \left[A_{\alpha x}^{\mathcal{I}},\ A_{\alpha y}^{\mathcal{I}},\ A_{\alpha z}^{\mathcal{I}}\right]^T$	Payload acceleration induced by the rotation of α
$\boldsymbol{A}_{\beta}^{\mathcal{I}} = \left[A_{\beta x}^{\mathcal{I}},\ A_{\beta y}^{\mathcal{I}},\ A_{\beta z}^{\mathcal{I}}\right]^T$	Payload acceleration induced by the rotation of β
$\boldsymbol{A}_{\delta}^{\mathcal{I}} = \left[A_{\delta x}^{\mathcal{I}},\ A_{\delta y}^{\mathcal{I}},\ A_{\delta z}^{\mathcal{I}}\right]^T$	Payload acceleration induced by the rotation of δ
$\boldsymbol{A}_{Q}^{\mathcal{I}} = \left[A_{Qx}^{\mathcal{I}},\ A_{Qy}^{\mathcal{I}},\ A_{Qz}^{\mathcal{I}}\right]^T$	Acceleration of the midpoint of the two quadrotors
$\boldsymbol{A}_{iQ}^{\mathcal{I}} = \left[A_{iQx}^{\mathcal{I}},\ A_{iQy}^{\mathcal{I}},\ A_{iQz}^{\mathcal{I}}\right]^T$	Acceleration of the i-th quadrotor

Table 2. Quadrotor–payload system parameter definitions and nominal values.

Symbol	Description of parameter	Standard/Nominal value
mq	Mass of the quadrotor vehicle	1 kg
mp	Mass of the attached payload	0.05 kg
l	Cable length between the payload and the knot	0.5 m
lq	Cable length linking the quadrotor to the knot	0.707 m

© 2023 The Author(s). | Published by Agro Intelligence Research Press

JBx, JBy, JBz	Moments of inertia of the quadrotor body	0.01 kg·m²
Jr	Inertia moment of the rotor	3.789 × 10−6 kg·m²
K	Coefficient representing aerodynamic drag	0.04 kg/m
g	Acceleration due to gravity	9.8 m/s²

Frame setup

A right-hand orientation convention governs all rotational quantities—angles, rates, and accelerations alike—considered in this study. The cooperative transport configuration under examination features a pair of cables descending from the two rotorcraft and converging at a junction, thereby forming a "Y"-shaped suspension geometry. To capture the motion of this coupled system, a collection of coordinate frames is established, each obeying the right-hand rule. **Figure 2** illustrates. The inertial reference is designated I = {x_I, y_I, z_I}. Attached to the i-th quadrotor is the body frame $^{B}_{i}$ = {x_{Bi}, y_{Bi}, z_{Bi} }. A translated copy of the inertial frame, shown in blue and labeled I′ = {x_I', y_I', z_I'}, has its origin at the midpoint between the two vehicles. The purple frame $^{L}_{1}$ = {x_{L1}, y_{L1}, z_{L1}} is co-located with I′ but reoriented such that yL1 aims toward Quadrotor 1 while zL1 points earthward. The angular offset about the z′I-axis that brings I′ into coincidence with L1 is termed δ and referred to as the formation yaw angle. Under nominal flight, progression occurs along xL1; however, as Section 4.3 discusses, constrained environments—such as narrow corridors—may compel travel along yL1 instead. A subsequent rotation of L1 about its yL1-axis by the amount α produces the frame L = {x_L, y_L, z_L}, also colored purple. This frame plays a central role in deriving the payload swing in Section 2.3.

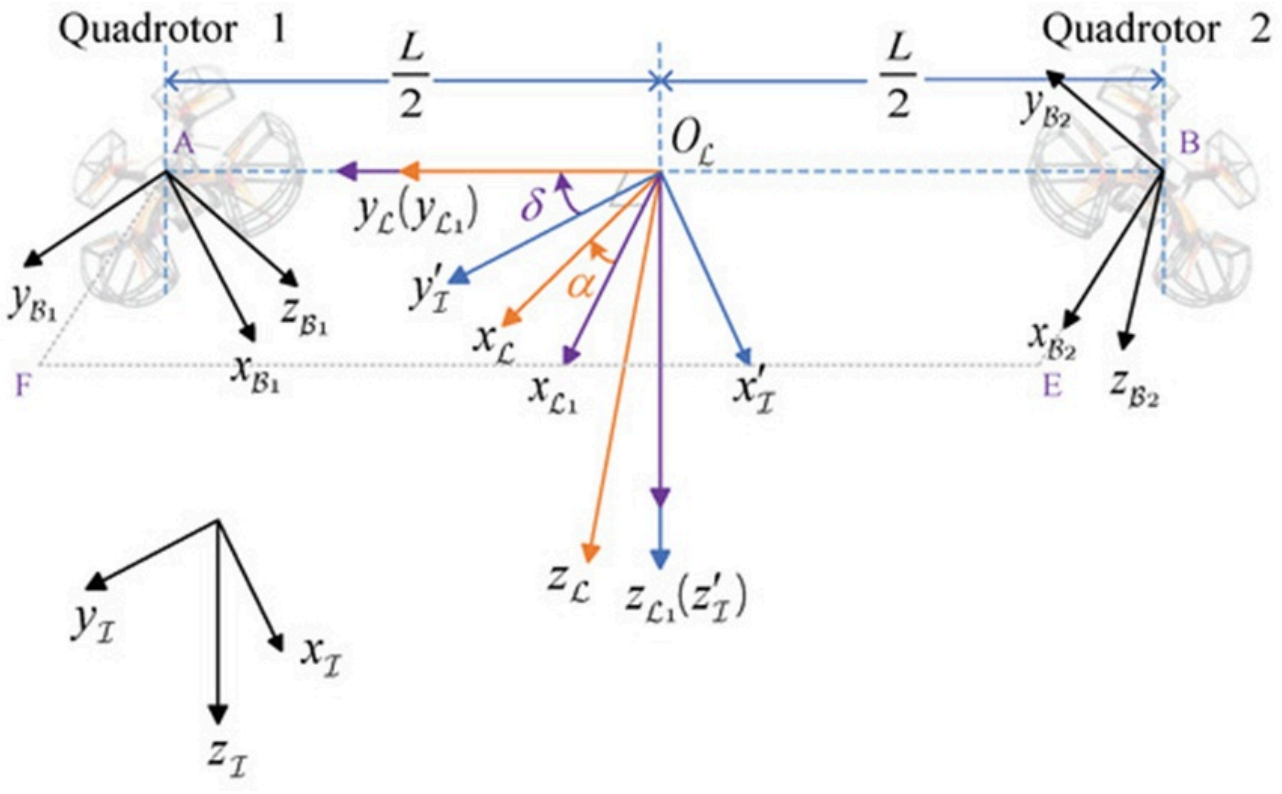

Figure 2. Frames for the modeling.

Modeling of quadrotors

The principles of linear momentum and angular momentum provide the foundation for the quadrotor equations of motion. Translational dynamics follow:

© 2023 The Author(s). | Published by Agro Intelligence Research Press

$$\begin{cases} \dot{V}_{ix}^{\mathcal{B}} = \frac{F_{iDqx}^{\mathcal{B}}}{m_q} + V_{iy}^{\mathcal{B}}\omega_{iz}^{\mathcal{B}} - V_{iz}^{\mathcal{B}}\omega_{iy}^{\mathcal{B}} - g\sin\theta_i, \\ \dot{V}_{iy}^{\mathcal{B}} = \frac{F_{iDqy}^{\mathcal{B}}}{m_q} + V_{iz}^{\mathcal{B}}\omega_{ix}^{\mathcal{B}} - V_{ix}^{\mathcal{B}}\omega_{iz}^{\mathcal{B}} + g\cos\theta_i\sin\phi_i, \\ \dot{V}_{iz}^{\mathcal{B}} = -\frac{F_{iqz}^{\mathcal{B}}}{m_q} + \frac{F_{iDqz}^{\mathcal{B}}}{m_q} + V_{ix}^{\mathcal{B}}\omega_{iy}^{\mathcal{B}} - V_{iy}^{\mathcal{B}}\omega_{ix}^{\mathcal{B}} + g\cos\theta_i\cos\phi_i, \end{cases} \quad (1)$$

In which the net perturbing force experienced by the i-th vehicle is expressed as:

$$\boldsymbol{F}_{iDq}^{\mathcal{B}} = \boldsymbol{F}_{iaq}^{\mathcal{B}} + \boldsymbol{R}_{\mathcal{J}}^{\mathcal{B}}\boldsymbol{T}_i^{\mathcal{J}}, \quad (2)$$

The aerodynamic resistance contribution within this expression reads:

$$\boldsymbol{F}_{iaq}^{\mathcal{B}} = \boldsymbol{R}_{\mathcal{J}}^{\mathcal{B}}\left(-\frac{1}{2}K\left\|\boldsymbol{V}_i^{\mathcal{J}}\right\|_2\boldsymbol{V}_i^{\mathcal{J}}\right), \quad (3)$$

And $\boldsymbol{T}^{\mathcal{J}}_i$ captures the tether-imparted tensile load on the i-th aircraft, a quantity elaborated in Section 2.3. The orientation mapping that takes vectors from the body frame into the inertial frame is denoted:

$$\boldsymbol{R}_{\mathcal{B}}^{\mathcal{I}} = (\boldsymbol{R}_{\mathcal{I}}^{\mathcal{B}})^T = \begin{bmatrix} \cos\theta_i\cos\psi_i & \sin\phi_i\sin\theta_i\cos\psi_i - \sin\psi_i\cos\phi_i & \cos\phi_i\sin\theta_i\cos\psi_i + \sin\psi_i\sin\phi_i \\ \cos\theta_i\sin\psi_i & \sin\phi_i\sin\theta_i\sin\psi_i + \cos\psi_i\cos\phi_i & \cos\phi_i\sin\theta_i\sin\psi_i - \cos\psi_i\sin\phi_i \\ -\sin\theta_i & \cos\theta_i\sin\phi_i & \cos\theta_i\cos\phi_i \end{bmatrix}. \quad (4)$$

Rotational motion and the associated kinematic relationships are captured by:

$$\begin{cases} \dot{\omega}_{ix}^{\mathcal{B}} = \frac{1}{J_x^{\mathcal{B}}}(\tau_{ix}^{\mathcal{B}} + J_y^{\mathcal{B}}\omega_{iy}^{\mathcal{B}}\omega_{iz}^{\mathcal{B}} - J_z^{\mathcal{B}}\omega_{iy}^{\mathcal{B}}\omega_{iz}^{\mathcal{B}} - J_r\omega_{iy}^{\mathcal{B}}\Omega_i), \\ \dot{\omega}_{iy}^{\mathcal{B}} = \frac{1}{J_y^{\mathcal{B}}}(\tau_{iy}^{\mathcal{B}} + J_z^{\mathcal{B}}\omega_{ix}^{\mathcal{B}}\omega_{iz}^{\mathcal{B}} - J_x^{\mathcal{B}}\omega_{ix}^{\mathcal{B}}\omega_{iz}^{\mathcal{B}} + J_r\omega_{ix}^{\mathcal{B}}\Omega_i), \\ \dot{\omega}_{iz}^{\mathcal{B}} = \frac{1}{J_z^{\mathcal{B}}}(\tau_{iz}^{\mathcal{B}} + J_x^{\mathcal{B}}\omega_{ix}^{\mathcal{B}}\omega_{iy}^{\mathcal{B}} - J_y^{\mathcal{B}}\omega_{ix}^{\mathcal{B}}\omega_{iy}^{\mathcal{B}}), \end{cases} \quad (5)$$

$$\begin{cases} \dot{\phi}_i = \omega_{ix}^{\mathcal{B}} + \tan\theta_i(\omega_{iy}^{\mathcal{B}}\sin\phi_i + \omega_{iz}^{\mathcal{B}}\cos\phi_i), \\ \dot{\theta}_i = \omega_{iy}^{\mathcal{B}}\cos\phi_i - \omega_{iz}^{\mathcal{B}}\sin\phi_i, \\ \dot{\psi}_i = \frac{1}{\cos\theta_i}(\omega_{iy}^{\mathcal{B}}\sin\phi_i + \omega_{iz}^{\mathcal{B}}\cos\phi_i). \end{cases} \quad (6)$$

Modeling of payload motion

© 2023 The Author(s). | Published by Agro Intelligence Research Press

Figure 3 offers the clearest depiction of the suspended object's behavior. The overall oscillation is resolved into two constituent stages, each quantified by a dedicated angular variable: α and β. For analytical tractability, the cables and their junction are taken to be without mass, an idealization that imposes a coplanar arrangement among the load Pi, the junction Oi, and the two quadrotors A and B. Within the first stage—termed forward–backward—the swing angle α tilts the vertical plane ABNM into alignment with plane ABCD via rotation around yL, relocating the junction from O1 to O2 and the load from P1 to P2. The second, lateral stage involves angle β rotating the segment O2P2 about the axis xL′ (parallel to xL) within plane ABCD, thereby moving the load from P2 to P3.

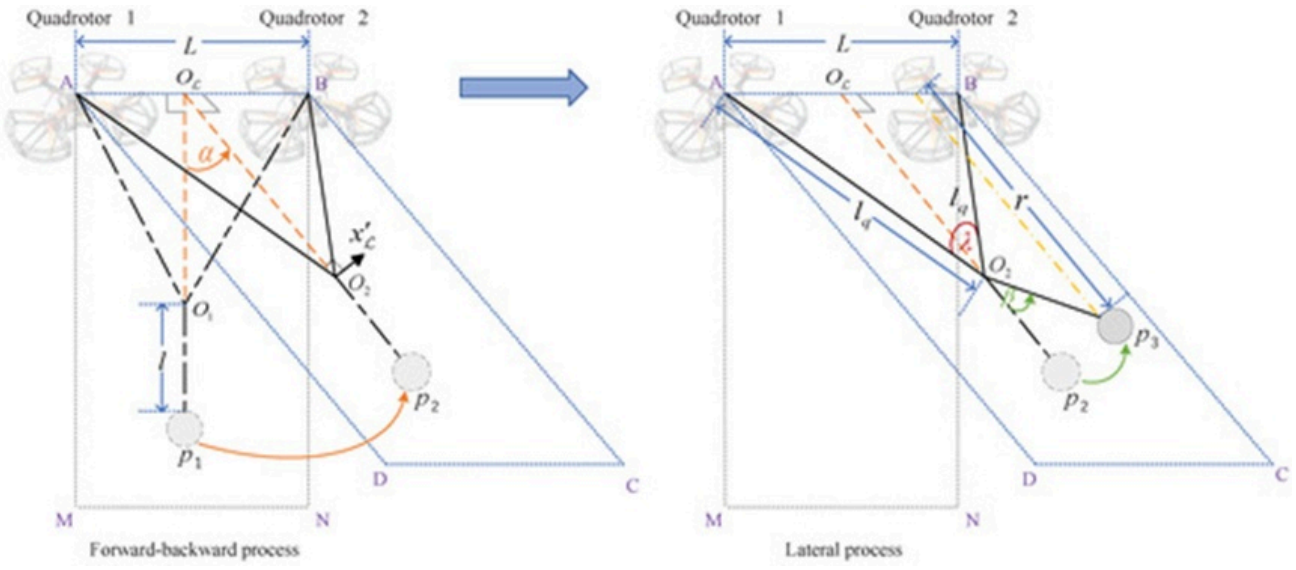

Figure 3. The forward–backward, and lateral processes of the "Y"-shaped cable-suspended payload swing motion.

Applying Newton's second law to the load yields:

$$\boldsymbol{T}_p^{\mathcal{I}} + \boldsymbol{G}_p^{\mathcal{I}} + \boldsymbol{F}_{Dp}^{\mathcal{I}} = m_p(\boldsymbol{A}_Q^{\mathcal{I}} + \boldsymbol{A}_\delta^{\mathcal{I}} + \boldsymbol{A}_\alpha^{\mathcal{I}} + \boldsymbol{A}_\beta^{\mathcal{I}}), \tag{7}$$

$$F_{Dp}^{\mathcal{J}} = -\frac{1}{2}K\left\|V_p^{\mathcal{J}}\right\|_2 V_p^{\mathcal{J}}$$

Where $\boldsymbol{T}_p^{\mathcal{I}}$ denotes the tensile force transmitted through the tether, to be formulated below; $\boldsymbol{G}_p^{\mathcal{I}} = [0\ 0\ m_p g]^T$ is the gravitational contribution;

$F_{Dp}^{\mathcal{I}} = -\frac{1}{2}K\left\|V_p^{\mathcal{I}}\right\|_2 V_p^{\mathcal{I}}$ accounts for aerodynamic drag; and the terms $\boldsymbol{A}_Q^{\mathcal{I}}$, $\boldsymbol{A}_\delta^{\mathcal{I}}$, $\boldsymbol{A}_\alpha^{\mathcal{I}}$, and $\boldsymbol{A}_\beta^{\mathcal{I}}$ represent acceleration components experienced by the load relative to $\mathcal{I}$, stemming, respectively, from linear motion of O$\mathcal{L}$ and from rotations involving δ, α, and β. These are given explicitly as:

$$\boldsymbol{A}_Q^{\mathcal{I}} = \frac{1}{2}(\boldsymbol{A}_{Q1}^{\mathcal{I}} + \boldsymbol{A}_{Q2}^{\mathcal{I}}), \tag{8}$$

© 2023 The Author(s). | Published by Agro Intelligence Research Press

$$A_{\delta}^{\mathcal{I}} = -\dot{\delta}^2 r_{\delta}^{\mathcal{I}} + \ddot{\delta}^{\mathcal{I}} \times r_{\delta}^{\mathcal{I}}, \quad (9)$$

$$A_{\alpha}^{\mathcal{I}} = -\dot{\alpha}^2 r^{\mathcal{I}} + \ddot{\alpha}^{\mathcal{I}} \times r^{\mathcal{I}}, \quad (10)$$

$$A_{\beta}^{\mathcal{I}} = -\dot{\beta}^2 l^{\mathcal{I}} + \ddot{\beta}^{\mathcal{I}} \times l^{\mathcal{I}}. \quad (11)$$

In the acceleration **Eqs. 9–11**, the first grouping of terms corresponds to centripetal effects, the second to tangential effects.

To streamline manipulations, we elect to formulate both the tether force and the acceleration contributions in $\mathcal{L}$ first, subsequently transforming them to $\mathcal{I}$ using the rotation matrix.

$$R_{\mathcal{I}}^{\mathcal{L}} = (R_{\mathcal{L}}^{\mathcal{I}})^T = \begin{bmatrix} \cos\alpha\cos\delta & \cos\alpha\sin\delta & -\sin\alpha \\ -\sin\delta & \cos\delta & 0 \\ \sin\alpha\cos\delta & \sin\alpha\sin\delta & \cos\alpha \end{bmatrix} \quad (12)$$

From the geometry sketched in **Figure 3**, one readily establishes that the tensile force vector exerted on the suspended object relates to the scalar tension magnitude Tp according to:

$$T_p^{\mathcal{L}} = T_p \begin{bmatrix} 0 \\ \sin\beta \\ -\cos\beta \end{bmatrix}. \quad (13)$$

Additionally, the vector $\boldsymbol{r}^{\mathrm{L}}$ is defined within L: it has magnitude r, lies perpendicular to segment AB, and points toward the load. Similarly, $\boldsymbol{l}^{\mathrm{L}}$ is a vector in L with magnitude l, originating at the junction and terminating at the load. The vector $\boldsymbol{r}_{\delta}^{\mathrm{l}}$, meanwhile, is orthogonal to the z_{l}'-axis, its magnitude equals the radial distance from the load to that axis, and it points outward from the axis toward the load.

These definitions imply the following geometric constraints:

$$r^{\mathcal{L}} = r\begin{bmatrix} 0 \\ 0 \\ 1 \end{bmatrix}, \; l^{\mathcal{L}} = l\begin{bmatrix} 0 \\ -\sin\beta \\ \cos\beta \end{bmatrix}, \; r_{\delta}^{\mathcal{L}} = \begin{bmatrix} r\sin\alpha\cos\alpha \\ -l\sin\beta \\ r\sin^2\alpha \end{bmatrix}, \quad (14)$$

Where:

© 2023 The Author(s). | Published by Agro Intelligence Research Press

$$r = l_q \cos\frac{\lambda}{2} + l\cos\beta,\ \ \lambda = \arccos\left(\frac{2l_q^2 - L^2}{2l_q^2}\right). \tag{15}$$

It should be noted that **Eq. 15** treats L as fixed, an assumption that greatly simplifies the derivation of the payload model. During controller design, on the other hand, L may be regarded as adjustable over time, governing the variable formation scale of the system—a capability with tangible value when negotiating real-world obstacles.

Combining **Eqs. 7-15** and carrying out the necessary algebraic steps furnishes the explicit dynamic equations for the two swing angles and the tether tension:

$$\begin{aligned}
\ddot{\alpha} = \frac{1}{r}\{&-g\sin\alpha - [\frac{1}{2}(A^{\mathcal{I}}_{1Qx} + A^{\mathcal{I}}_{2Qx}) - \dot{\delta}^2(r\sin\alpha\cos\delta + l\sin\beta\sin\delta) - \ddot{\delta}(r\sin\alpha\sin\delta - l\sin\beta\cos\delta)\\
&-\frac{F^{\mathcal{I}}_{Dpx}}{m_p}]\cos\alpha\cos\delta - [\frac{1}{2}(A^{\mathcal{I}}_{1Qy} + A^{\mathcal{I}}_{2Qy}) - \dot{\delta}^2(r\sin\alpha\sin\delta - l\sin\beta\cos\delta) + \ddot{\delta}(r\sin\alpha\cos\delta + l\sin\beta\sin\delta)\\
&-\frac{F^{\mathcal{I}}_{Dpy}}{m_p}]\cos\alpha\sin\delta + [\frac{1}{2}(A^{\mathcal{I}}_{1Qz} + A^{\mathcal{I}}_{2Qz}) - \frac{F^{\mathcal{I}}_{Dpz}}{m_p}]\sin\alpha\},\\
\ddot{\beta} = \frac{1}{l}\{&-\dot{\alpha}^2 r\sin\beta - g\cos\alpha\sin\beta + [\frac{1}{2}(A^{\mathcal{I}}_{1Qx} + A^{\mathcal{I}}_{2Qx}) - \dot{\delta}^2(r\sin\alpha\cos\delta + l\sin\beta\sin\delta) - \ddot{\delta}(r\sin\alpha\sin\delta - l\sin\beta\cos\delta)\\
&-\frac{F^{\mathcal{I}}_{Dpx}}{m_p}](\sin\alpha\sin\beta\cos\delta - \cos\beta\sin\delta) + [\frac{1}{2}(A^{\mathcal{I}}_{1Qy} + A^{\mathcal{I}}_{2Qy}) - \dot{\delta}^2(r\sin\alpha\sin\delta - l\sin\beta\cos\delta) + \ddot{\delta}(r\sin\alpha\cos\delta
\end{aligned} \tag{16}$$

$$\begin{aligned}
&+l\sin\beta\sin\delta) - \frac{F^{\mathcal{I}}_{Dpy}}{m_p}](\sin\alpha\sin\beta\sin\delta + \cos\beta\cos\delta) + [\frac{1}{2}(A^{\mathcal{I}}_{1Qz} + A^{\mathcal{I}}_{2Qz}) - \frac{F^{\mathcal{I}}_{Dpz}}{m_p}]\cos\alpha\sin\beta\},\\
T_p = m_p\{&\dot{\alpha}^2 r\cos\beta + \dot{\beta}^2 l + g\cos\alpha\cos\beta - [\frac{1}{2}(A^{\mathcal{I}}_{1Qx} + A^{\mathcal{I}}_{2Qx}) - \dot{\delta}^2(r\sin\alpha\cos\delta + l\sin\beta\sin\delta) - \ddot{\delta}(r\sin\alpha\sin\delta\\
&-l\sin\beta\cos\delta) - \frac{F^{\mathcal{I}}_{Dpx}}{m_p}](\sin\beta\sin\delta + \sin\alpha\cos\beta\cos\delta) + [\frac{1}{2}(A^{\mathcal{I}}_{1Qy} + A^{\mathcal{I}}_{2Qy}) - \dot{\delta}^2(r\sin\alpha\sin\delta - l\sin\beta\cos\delta)
\end{aligned} \tag{17}$$

$$+\ddot{\delta}(r\sin\alpha\cos\delta + l\sin\beta\sin\delta) - \frac{F^{\mathcal{I}}_{Dpy}}{m_p}](\sin\beta\cos\delta - \sin\alpha\cos\beta\sin\delta) - [\frac{1}{2}(A^{\mathcal{I}}_{1Qz} + A^{\mathcal{I}}_{2Qz}) - \frac{F^{\mathcal{I}}_{Dpz}}{m_p}]\cos\alpha\cos\beta\}. \tag{18}$$

Newton's third law dictates that the force on the junction opposes the force on the aircraft. Leveraging the spatial relationships between the quadrotors and the load, the cable forces acting on the i-th quadrotor are obtained as:

$$T_1 = -\frac{T_p}{2}\left(\frac{\sin\beta + \cos\beta\tan\frac{\lambda}{2}}{\sin\frac{\lambda}{2}}\right), \tag{19}$$

© 2023 The Author(s). | Published by Agro Intelligence Research Press

$$T_2 = -T_p\left(\frac{\cos\beta}{\cos\frac{\lambda}{2}} - \frac{\sin\beta + \cos\beta\tan\frac{\lambda}{2}}{2\sin\frac{\lambda}{2}}\right). \quad (20)$$

From here, expressing the force vector in $\mathcal{L}$ and applying the mapping $\boldsymbol{R}^{\mathcal{J}}{}_{\mathcal{L}}$ yields the desired cable force vectors on each quadrotor:

$$T_1^{\mathcal{I}} = T_1\begin{bmatrix} -\sin\delta\sin\frac{\lambda}{2} - \sin\alpha\cos\delta\cos\frac{\lambda}{2} \\ \cos\delta\sin\frac{\lambda}{2} - \sin\alpha\sin\delta\cos\frac{\lambda}{2} \\ -\cos\alpha\cos\frac{\lambda}{2} \end{bmatrix}, \quad (21)$$

$$T_2^{\mathcal{I}} = T_2\begin{bmatrix} \sin\delta\sin\frac{\lambda}{2} - \sin\alpha\cos\delta\cos\frac{\lambda}{2} \\ -\cos\delta\sin\frac{\lambda}{2} - \sin\alpha\sin\delta\cos\frac{\lambda}{2} \\ -\cos\alpha\cos\frac{\lambda}{2} \end{bmatrix}. \quad (22)$$

Model simplification

The mutual coupling and nonlinearity of the quadrotor and payload descriptions pose an obstacle to straightforward controller synthesis. We therefore decompose the integrated system into six independent channels to facilitate the design procedure.

Initially, by imposing the small-angle assumptions:

$$\sin\theta_i = \sin\phi_i = 0, \quad \cos\theta_i = \cos\phi_i = 1 \quad (23)$$

On the rotational **Eqs. 5 and 6**, and by treating the translational motion under a point-mass approximation (1), the inertial-frame quadrotor behavior can be rendered approximately as:

$$\begin{cases} \ddot{\phi}_i = \frac{1}{J_x^{\mathcal{B}}}(\tau_{ix}^{\mathcal{B}} + J_y^{\mathcal{B}}\dot{\theta}_i\dot{\psi}_i - J_z^{\mathcal{B}}\dot{\theta}_i\dot{\psi}_i - J_r\dot{\theta}_i\Omega_i), \\ \ddot{\theta}_i = \frac{1}{J_y^{\mathcal{B}}}(\tau_{iy}^{\mathcal{B}} + J_z^{\mathcal{B}}\dot{\phi}_i\dot{\psi}_i - J_x^{\mathcal{B}}\dot{\phi}_i\dot{\psi}_i + J_r\dot{\phi}_i\Omega_i), \\ \ddot{\psi}_i = \frac{1}{J_z^{\mathcal{B}}}(\tau_{iz}^{\mathcal{B}} + J_x^{\mathcal{B}}\dot{\phi}_i\dot{\theta}_i - J_y^{\mathcal{B}}\dot{\phi}_i\dot{\theta}_i), \end{cases} \quad (24)$$

© 2023 The Author(s). | Published by Agro Intelligence Research Press

$$\begin{cases} A^{\mathcal{I}}_{iQx} = \ddot{x}^I_i = -\frac{1}{m_q}\left(F^{\mathcal{B}}_{iqz}\sin\phi_i\sin\psi_i + F^{\mathcal{B}}_{iqz}\cos\phi_i\sin\theta_i\cos\psi_i + d^I_{ix}\right), \\ A^{\mathcal{I}}_{iQy} = \ddot{y}^I_i = -\frac{1}{m_q}\left(-F^{\mathcal{B}}_{iqz}\sin\phi_i\cos\psi_i + F^{\mathcal{B}}_{iqz}\cos\phi_i\sin\theta_i\sin\psi_i + d^I_{iy}\right), \\ A^{\mathcal{I}}_{iQz} = \ddot{z}^I_i = -\frac{1}{m_q}\left(F^{\mathcal{B}}_{iqz}\cos\phi_i\cos\psi_i + d^I_{iz}\right) + g, \end{cases} \quad (25)$$

Where the term $d^{\mathcal{I}} = R^{\mathcal{I}}_{\mathcal{B}} F^{\mathcal{B}}_{Dq}$ consolidates the complete disturbance, spanning aerodynamic drag together with perturbations induced by the load's gravitational and oscillatory influences.

Subsequently, feedback linearization is applied to **Eqs. 24 and 25** to secure further simplification. Introducing the synthetic control actions:

$$\begin{cases} u_{i\phi} = \frac{1}{J^{\mathcal{B}}_x}\tau^{\mathcal{B}}_{ix}, \\ u_{i\theta} = \frac{1}{J^{\mathcal{B}}_y}\tau^{\mathcal{B}}_{iy}, \\ u_{i\psi} = \frac{1}{J^{\mathcal{B}}_z}\tau^{\mathcal{B}}_{iz}, \\ u_{ix} = -\frac{1}{m_q}\left(F^{\mathcal{B}}_{iqz}\sin\phi_i\sin\psi_i + F^{\mathcal{B}}_{iqz}\cos\phi_i\sin\theta_i\cos\psi_i\right), \\ u_{iy} = -\frac{1}{m_q}\left(-F^{\mathcal{B}}_{iqz}\sin\phi_i\cos\psi_i + F^{\mathcal{B}}_{iqz}\cos\phi_i\sin\theta_i\sin\psi_i\right), \\ u_{iz} = -\frac{1}{m_q}F^{\mathcal{B}}_{iqz}\cos\phi_i\cos\psi_i + g, \end{cases} \quad (26)$$

Alongside the lumped disturbance quantities:

$$\begin{cases} f_{i\phi} = \frac{1}{J^{\mathcal{B}}_x}\left(J^{\mathcal{B}}_y\dot{\theta}_i\dot{\psi}_i - J^{\mathcal{B}}_z\dot{\theta}_i\dot{\psi}_i - J_r\dot{\theta}_i\Omega_i\right), \\ f_{i\theta} = \frac{1}{J^{\mathcal{B}}_y}\left(J^{\mathcal{B}}_z\dot{\phi}_i\dot{\psi}_i - J^{\mathcal{B}}_x\dot{\phi}_i\dot{\psi}_i + J_r\dot{\phi}_i\Omega_i\right), \\ f_{i\psi} = \frac{1}{J^{\mathcal{B}}_z}\left(J^{\mathcal{B}}_x\dot{\phi}_i\dot{\theta}_i - J^{\mathcal{B}}_y\dot{\phi}_i\dot{\theta}_i\right), \\ f_{ix} = -\frac{1}{m_q}d^{\mathcal{I}}_{ix}, \\ f_{iy} = -\frac{1}{m_q}d^{\mathcal{I}}_{iy}, \\ f_{iz} = -\frac{1}{m_q}d^{\mathcal{I}}_{iz}, \end{cases} \quad (27)$$

Transforms **Eqs. 24 and 25** into a set of second-order single-degree-of-freedom systems taking the form:

$$\begin{cases} \ddot{\xi}_i = u^{\xi}_i + f^{\xi}_i, \\ \ddot{\eta}_i = u^{\eta}_i + f^{\eta}_i, \end{cases} \quad (28)$$

© 2023 The Author(s). | Published by Agro Intelligence Research Press

In which $\boldsymbol{\xi}i = [\psi i, x_i, y_i, z_i]^T$ and $\boldsymbol{\eta}i = [\boldsymbol{\phi}i, \theta i]^T$ are the state vectors, $\boldsymbol{u}_i^{\xi} = [u_i^{\psi}, u_i^{x}, u_i^{y}, u_i^{z}]^T$ and $\boldsymbol{u}_i^{\eta} = [u_i^{\phi}, u_i^{\theta}]^T$ serve as the synthetic input vectors, and $\boldsymbol{f}_i^{\xi} = [f_i^{\psi}, f_i^{x}, f_i^{y}, f_i^{z}]^T$ together with $\boldsymbol{f}_i^{\eta} = [f_i^{\phi}, f_i^{\theta}]^T$ constitute the aggregate disturbance vectors.

Communication topology and control objectives

Figure 4 portrays the information-exchange architecture that couples the two quadrotors with the global reference source. In this configuration, the reference signals—namely, the commanded trajectory PdI and the commanded formation yaw angle δd—are supplied exclusively to Quadrotor 1. Between themselves, the two vehicles may freely exchange state data, control commands, and the desired formation scale Ld via the communication channel. Throughout the remainder of the document, attaching the subscript “d” to any variable denotes its reference or commanded value.

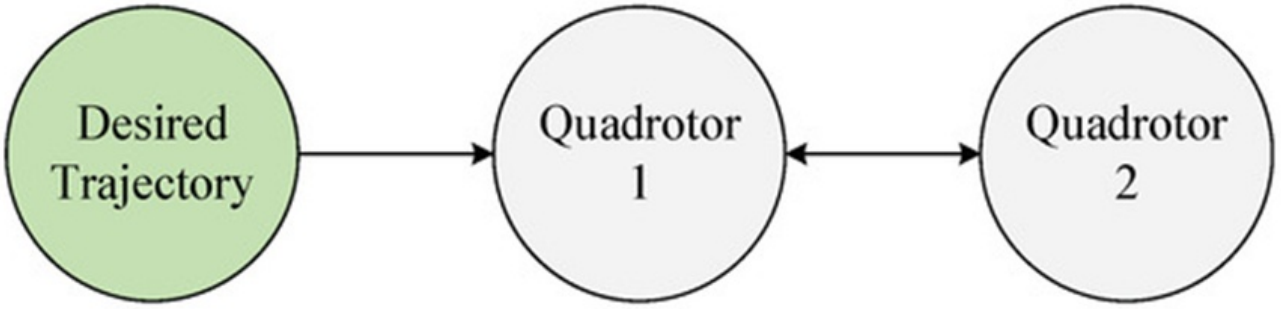

Figure 4. The communication network topology.

The objectives that the guidance law and robust cooperative controller developed in this paper must fulfill, under the communication constraints depicted in **Figure 4**, are enumerated as follows:

(i) The yaw angles of the two quadrotors converge to the commanded formation yaw angle in a synchronized manner, i.e., $(t) \rightarrow \delta d(t)$ as $t \rightarrow \infty$;

(ii) When disturbances are absent, asymptotic tracking of the prescribed trajectory is achieved while the quadrotors maintain the commanded formation geometry—potentially time-varying—specified by $Ld(t)$;

(iii) Under the influence of disturbances, both the trajectory-following deviation and the formation mismatch are quantitatively confined to an arbitrarily narrow band around zero.

Guidance and Robust Control Design

Figure 5 portrays the dual-component scheme we advance to meet the prescribed control specifications.

© 2023 The Author(s). | Published by Agro Intelligence Research Press

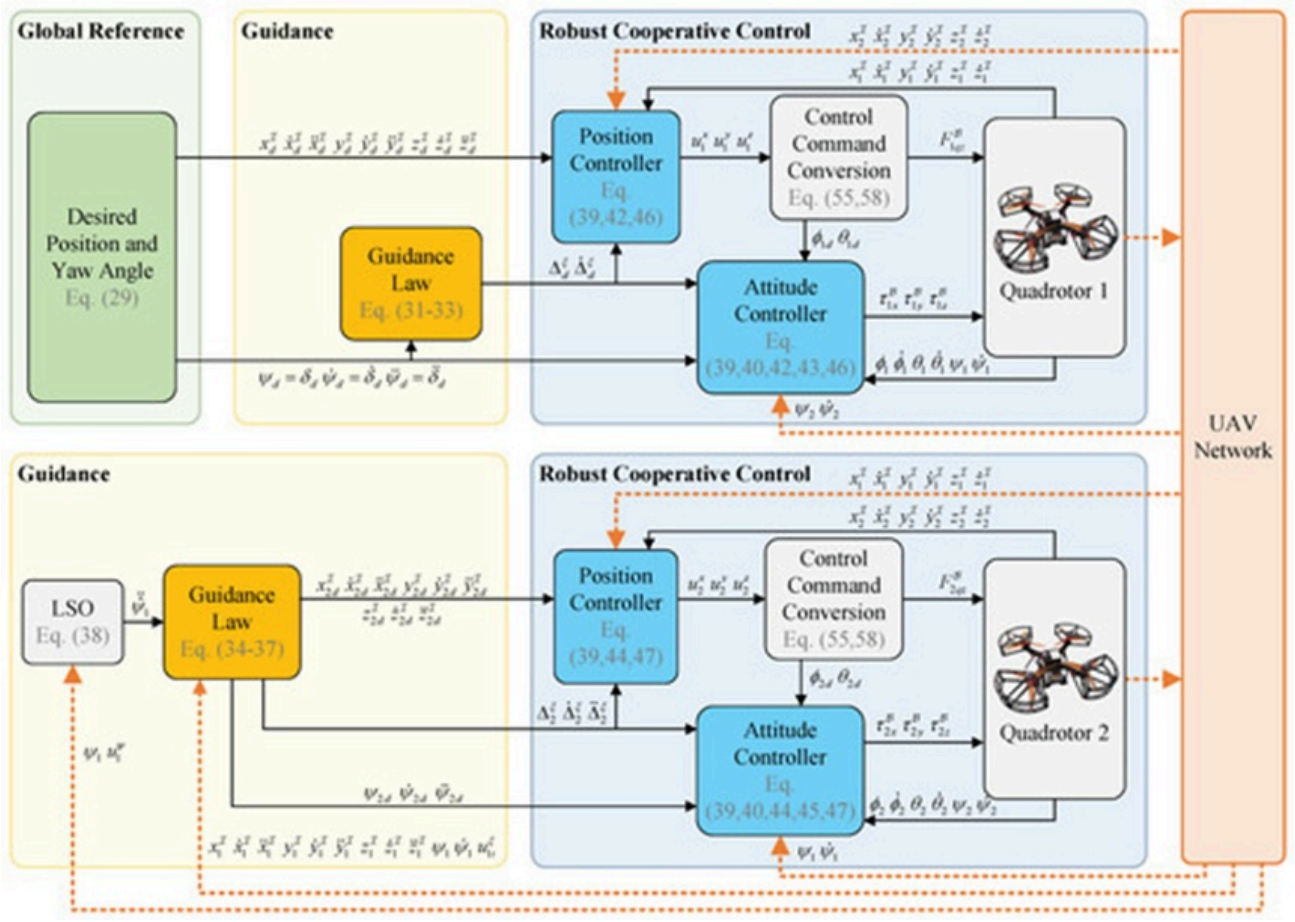

Figure 5. The proposed guidance and robust cooperative control scheme for the quadrotor formation.

The guidance component shoulders two responsibilities. Its first task is to translate the commanded formation quantities —namely, the yaw angle δd and the separation distance Ld—into a formation offset that feeds the cooperative control module, thereby enabling the pair of vehicles to assume the required geometry. Its second task, indispensable for Quadrotor 2, is to synthesize local reference trajectories that compensate for the inaccessibility of the global desired path due to the communication structure shown in **Figure 4**.

Turning to the robust control component, each quadrotor is equipped with a cooperative position regulator, an attitude regulator, a conversion stage that transforms high-level acceleration demands into low-level attitude-angle commands, and a thrust directive FiqzB. To counteract oscillatory disturbances transmitted from the suspended load, an uncertainty and disturbance estimator (UDE) that performs active cancellation is integrated into both the position and attitude regulation loops.

The subsequent subsections elaborate on the construction of each constituent.

Design of the guidance law

We commence by formalizing the global reference setup, after which the guidance law that furnishes Quadrotor 2 with its local reference is derived.

Let the global intended path for Quadrotor 1 be governed by:

© 2023 The Author(s). | Published by Agro Intelligence Research Press

$$\ddot{\xi}_{1d} = u_{1d}^{\xi}, \quad (29)$$

With $u_1{}^{\xi}{}_d$ representing the intended input. For a formation defined by inter-vehicle spacing Ld at orientation δd, the path prescribed for Quadrotor 2 becomes:

$$\begin{cases} \xi_{2d} = \xi_{1d} + \Delta_d^{\xi}, \\ \dot{\xi}_{2d} = \dot{\xi}_{1d} + \dot{\Delta}_d^{\xi}, \\ \ddot{\xi}_{2d} = u_{1d}^{\xi} + \ddot{\Delta}_d^{\xi}, \end{cases} \quad (30)$$

Where $\Delta^{\xi}{}_d$ captures the commanded formation displacement obeying:

$$\Delta_d^{\xi} = \begin{bmatrix} \Delta_d^{\psi} \\ \Delta_d^{x} \\ \Delta_d^{y} \\ \Delta_d^{z} \end{bmatrix} = \begin{bmatrix} 0 \\ L_d \sin \delta_d \\ -L_d \cos \delta_d \\ 0 \end{bmatrix}. \quad (31)$$

Successive differentiation of $\Delta^{\xi}{}_d$ produces:

$$\dot{\Delta}_d^{\xi} = \begin{bmatrix} \dot{\Delta}_d \\ \dot{\Delta}_d^{x} \\ \dot{\Delta}_d^{y} \\ \dot{\Delta}_d^{z} \end{bmatrix} = \begin{bmatrix} 0 \\ L_d \dot{\delta}_d \cos \delta_d + \dot{L}_d \sin \delta_d \\ L_d \dot{\delta}_d \sin \delta_d - \dot{L}_d \cos \delta_d \\ 0 \end{bmatrix} \quad (32)$$

And:

$$\ddot{\Delta}_d^{\xi} = \begin{bmatrix} \ddot{\Delta}_d^{\psi} \\ \ddot{\Delta}_d^{x} \\ \ddot{\Delta}_d^{y} \\ \ddot{\Delta}_d^{z} \end{bmatrix} = \begin{bmatrix} 0 \\ -L_d \dot{\delta}_d^2 \sin \delta_d + L_d \ddot{\delta}_d \cos \delta_d + \dot{L}_d \dot{\delta}_d \cos \delta_d + \ddot{L}_d \sin \delta_d + \dot{L}_d \dot{\delta}_d \cos \delta_d \\ L_d \dot{\delta}_d^2 \cos \delta_d + L_d \ddot{\delta}_d \sin \delta_d + \dot{L}_d \dot{\delta}_d \sin \delta_d - \ddot{L}_d \cos \delta_d + \dot{L}_d \dot{\delta}_d \sin \delta_d \\ 0 \end{bmatrix}. \quad (33)$$

The two aircraft must synchronize both heading angles and altitude throughout the formation maneuver.

For the ψ channel in particular, the assignment $\psi id = \delta d$ is enforced so that the heading of each vehicle coincides with the formation yaw angle.

© 2023 The Author(s). | Published by Agro Intelligence Research Press

While **Eqs. 29 and 30** constitute the "global" reference description dictated by the mission requirements, the communication architecture precludes Quadrotor 2 from directly receiving its global reference (30). This limitation compels us to devise a guidance law that assembles a "local" reference for Quadrotor 2 from information shared by Quadrotor 1—its states and input—together with the commanded formation datum Ld, in such a manner that the global objectives remain attainable. The strategy adopted herein is to replace every unavailable desired quantity appearing in **Eq. 30** with the matching state or control signal from Quadrotor 1. This yields the guidance law (i.e., the local reference destined for Quadrotor 2) expressed below:

$$\begin{cases} \xi_{2d}^{\star} = \xi_1 + \Delta_2^{\xi}, \\ \dot{\xi}_{2d}^{\star} = \dot{\xi}_1 + \dot{\Delta}_2^{\xi}, \\ \ddot{\xi}_{2d}^{\star} = u_{1t}^{\xi} + \ddot{\Delta}_2^{\xi}, \end{cases} \tag{34}$$

Where $\boldsymbol{u}_1{}^{\xi}{}_t$ denotes the trajectory-tracking portion of Quadrotor 1's control action, the design of which appears in Section 3.2, and the formation displacement substitutes ψ1 in place of δd and satisfies:

$$\boldsymbol{\Delta}_2^{\xi} = \begin{bmatrix} \Delta_2^{\psi} \\ \Delta_2^{x} \\ \Delta_2^{y} \\ \Delta_d^{z} \end{bmatrix} = \begin{bmatrix} 0 \\ L_d \sin \psi_1 \\ -L_d \cos \psi_1 \\ 0 \end{bmatrix}. \tag{35}$$

The associated first and second derivatives, Δ˙ 2ξ and Δ¨ 2ξ, then take the forms:

$$\dot{\boldsymbol{\Delta}}_2^{\xi} = \begin{bmatrix} \dot{\Delta}_2^{\psi} \\ \dot{\Delta}_2^{x} \\ \dot{\Delta}_2^{y} \\ \dot{\Delta}_2^{z} \end{bmatrix} = \begin{bmatrix} 0 \\ L_d\dot{\psi}_1 \cos \psi_1 + \dot{L}_d \sin \psi_1 \\ L_d\dot{\psi}_1 \sin \psi_1 - \dot{L}_d \cos \psi_1 \\ 0 \end{bmatrix} \tag{36}$$

And:

$$\ddot{\boldsymbol{\Delta}}_2^{\xi} = \begin{bmatrix} \ddot{\Delta}_2^{\psi} \\ \ddot{\Delta}_2^{x} \\ \ddot{\Delta}_2^{y} \\ \ddot{\Delta}_2^{z} \end{bmatrix} = \begin{bmatrix} 0 \\ -L_d\dot{\psi}_1^2 \sin \psi_1 + L_d\ddot{\psi}_1 \cos \psi_1 + \dot{L}_d\dot{\psi}_1 \cos \psi_1 + \dot{L}_d \sin \psi_1 + \dot{L}_d\dot{\psi}_1 \cos \psi_1 \\ L_d\dot{\psi}_1^2 \cos \psi_1 + L_d\ddot{\psi}_1 \sin \psi_1 + \dot{L}_d\dot{\psi}_1 \sin \psi_1 - \ddot{L}_d \cos \psi_1 + \dot{L}_d\dot{\psi}_1 \sin \psi_1 \\ 0 \end{bmatrix}. \tag{37}$$

© 2023 The Author(s). | Published by Agro Intelligence Research Press

A practical difficulty emerges from this guidance construction: the quantity ψ¨1 appearing in **Eq. 37** is not amenable to direct measurement. To surmount this, a Luenberger state observer (LSO) is deployed to generate an estimate of ψ¨1, denoted $\hat{\ddot{\psi}}_1$

$$\begin{bmatrix} \dot{\hat{\psi}}_1 \\ \ddot{\hat{\psi}}_1 \end{bmatrix} = \begin{bmatrix} -l_1 & 1 \\ -l_2 & 0 \end{bmatrix} \begin{bmatrix} \hat{\psi}_1 \\ \dot{\hat{\psi}}_1 \end{bmatrix} + \begin{bmatrix} l_1 \\ l_2 \end{bmatrix} \psi_1 + \begin{bmatrix} 0 \\ 1 \end{bmatrix} u_1^{\psi}, \quad (38)$$

Where ψˆ1 tracks ψ1; l1 and l2 designate the observer correction gains; and u1ψ is the control input elaborated in the section that follows.

Design of the robust controller

The control law must simultaneously secure three properties: (i) faithful pursuit of the global reference trajectory; (ii) preservation of the commanded formation geometry parameterized by Ld and δd; and (iii) attenuation of load-swing perturbations to ensure adequate robustness. To this end, the regulators for the ξ and η channels are structured, respectively, as:

$$u_i^{\xi} = u_{it}^{\xi} + u_{ic}^{\xi} - \hat{f}_i^{\xi}, \quad (39)$$

$$u_i^{\eta} = u_{it}^{\eta} - \hat{f}_i^{\eta}, \quad (40)$$

Where $\boldsymbol{u}_{it}^{\xi}$ and $\boldsymbol{u}_{it}^{\eta}$ constitute the trajectory-pursuit components, $\boldsymbol{u}_{ic}^{\xi}$ embodies the cooperative term that enforces the formation, and $\hat{\boldsymbol{f}}_i^{\xi}$ alongside $\hat{\boldsymbol{f}}_i^{\eta}$ denote the UDE-generated signals (derived in Section 3.3) that offset the disturbances.

Remark 1. Inspection of **Figure 5** reveals that the reference for the ξ channel is either the exogenous global specification **Eq. 29** or the locally generated surrogate (34). In contrast, the η channel—representing the inner tilt-angle regulation loop—derives its setpoints from acceleration commands issued by the ξ channel. The procedure for producing these inner-loop setpoints is termed “control command conversion” and receives dedicated treatment in Section 3.4.

The state tracking residuals are introduced as:

$$\begin{cases} \tilde{\xi}_i = \xi_{id} - \xi_i, \\ \tilde{\eta}_i = \eta_{id} - \eta_i. \end{cases} \quad (41)$$

Because Quadrotor 2 only possesses its local reference **Eq. 34**, the trajectory-pursuit regulators are formulated independently for each vehicle. For Quadrotor 1, these components read.

$$u_{1t}^{\xi} = u_{1d}^{\xi} + k_{1p}^{\xi} \tilde{\xi}_1 + k_{1d}^{\xi} \dot{\tilde{\xi}}_1, \quad (42)$$

© 2023 The Author(s). | Published by Agro Intelligence Research Press

$$u_{1t}^{\eta} = u_{1d}^{\eta} + k_{1p}^{\eta}\tilde{\eta}_1 + k_{1d}^{\eta}\dot{\tilde{\eta}}_1, \quad (43)$$

In which $u_1{}^{\xi}{}_d$ and $u_1{}^{\eta}{}_d$ function as feedforward contributions that drive the system along the nominal motion, ($k^{\xi}{}_{1p}\tilde{\boldsymbol{\xi}}_1$ + $k^{\xi}{}_{1d}\dot{\tilde{\boldsymbol{\xi}}}_1$) and ($k^{\eta}{}_{1p}\tilde{\boldsymbol{\eta}}_1$ + $k^{\eta}{}_{1d}\dot{\tilde{\boldsymbol{\eta}}}_1$) operate as feedback corrections that annihilate tracking discrepancies, and $k^{\xi}{}_{1p}$, $k^{\xi}{}_{1d}$, $k^{\eta}{}_{1p}$, and $k^{\eta}{}_{1d}$ are the corresponding gain coefficients. For Quadrotor 2, the trajectory-pursuit terms become:

$$u_{2t}^{\xi} = \ddot{\xi}_{2d}^{\star}, \quad (44)$$

$$u_{2t}^{\eta} = u_{2d}^{\eta} + k_{2p}^{\eta}\tilde{\eta}_1 + k_{2d}^{\eta}\dot{\tilde{\eta}}_2, \quad (45)$$

Where $\ddot{\xi}_2^{\star}\mathrm{d}$ supplies the feedforward command originating from the local reference mechanism **Eq. 34**.

To enforce cooperative formation flight, $\boldsymbol{u}_{ic}{}^{\xi}$ is shaped from the formation offsets $\boldsymbol{\Delta}^{\xi}{}_d$ (31) and $\boldsymbol{\Delta}_2{}^{\xi}$ (35) as:

$$u_{1c}^{\xi} = \alpha_1^{\xi}\left(\xi_2 - \xi_1 - \Delta_d^{\xi}\right) + \beta_1^{\xi}\left(\dot{\xi}_2 - \dot{\xi}_1 - \dot{\Delta}_d^{\xi}\right), \quad (46)$$

$$u_{2c}^{\xi} = \alpha_2^{\xi}\left(\xi_1 - \xi_2 + \Delta_2^{\xi}\right) + \beta_2^{\xi}\left(\dot{\xi}_1 - \dot{\xi}_2 + \dot{\Delta}_2^{\xi}\right), \quad (47)$$

With $\alpha_i{}^{\xi}$ and $\beta^{\xi}{}_i$ serving as the cooperative formation gains for the positional and velocity components, respectively.

Remark 2. In structuring Quadrotor 2's trajectory-pursuit law (44), we deliberately retain only a feedforward contribution. A feedback term anchored to the local reference system (34) as $k_{2p}^{\xi}(\xi_{2d}^{\star} - \xi_2) + k_{2d}^{\xi}(\dot{\xi}_{2d}^{\star} - \dot{\xi}_2)$, of the form k, would functionally duplicate the cooperative formation term $u_2{}^{\xi}{}_c$ specified in (47) and is therefore omitted for Quadrotor 2.

Design of UDE

To endow the quadrotors with resilience against load-sway perturbations, an uncertainty and disturbance estimator (UDE) is architected for each channel. Its function is to perform online estimation of the disturbance and subsequently inject the estimate for active cancellation. Owing to the identical structure shared by the models (28) for the ξ and η channels, it suffices to develop the UDE for the ξ channel alone; the results extend to the η channel without alteration, and its treatment is consequently omitted for conciseness.

Following the canonical UDE-based control paradigm [17], the disturbance estimate $\hat{f}_i{}^{\xi}$ is required to fulfill, in the frequency domain and with reference to **Eq. 28**, the relation:

$$\hat{F}_i^{\xi}(s) = G_i^{\xi}(s)\,F_i^{\xi}(s) = G_i^{\xi}(s)\left[s^2\xi_i(s) - s\xi_i(0) - \dot{\xi}_i(0) - U_i^{\xi}(s)\right], \quad (48)$$

© 2023 The Author(s). | Published by Agro Intelligence Research Press

Where capital letters signify Laplace-transformed quantities; $\boldsymbol{G}_i^{\xi}(s) = diag\{G_i^{\psi}(s), G_i^{x}(s), G_i^{y}(s), G_i^{z}(s)\}$ constitutes a transfer function matrix that embodies a design degree of freedom inherent to the UDE; and G_i^{ξ} (s), ξ ∈ {ψ, x, y, z} are strictly proper, stable, rational transfer functions whose specification is deferred.

Assuming quiescent initial conditions and substituting **Eqs. 39 into 48** yields:

$$\hat{F}_i^{\xi}(s) = G_i^{\xi}(s)\left[s^2\xi_i(s) - U_{it}^{\xi}(s) - U_{ic}^{\xi}(s) + \hat{F}_i^{\xi}(s)\right]. \quad (49)$$

Extracting $\hat{\boldsymbol{F}}_i^{\xi}(s)$ from **Eq. 49** results in:

$$\hat{F}_i^{\xi}(s) = \left[I - G_i^{\xi}(s)\right]^{-1} G_i^{\xi}(s)\left[s^2\xi_i(s) - U_{it}^{\xi}(s) - U_{ic}^{\xi}(s)\right], \quad (50)$$

Where I denotes the identity matrix of compatible order. The role of $G_i^{\xi}(s)$ is to guarantee that $\hat{\boldsymbol{F}}_i^{\xi}(s)$ is physically realizable, motivating the choice:

$$G_i^{\xi}(s) = \frac{1}{T_i^{\xi}s + 1}, \quad \xi \in \{\psi, x, y, z\}, \quad (51)$$

With $T_i^{\xi} > 0$ dictating the UDE's estimation bandwidth. Inserting **Eqs. 51 into 50** delivers:

$$\hat{F}_i^{\xi}(s) = T_i^{\xi}\left[s\xi_i(s) - \frac{1}{s}\left(U_{it}^{\xi}(s) + U_{ic}^{\xi}(s)\right)\right], \quad (52)$$

Where the gain matrix is constrained by:

$$T_i^{\xi} = diag\left\{\frac{1}{T_i^{\psi}}, \frac{1}{T_i^{x}}, \frac{1}{T_i^{y}}, \frac{1}{T_i^{z}}\right\}. \quad (53)$$

Reverting **Eq. 52** to the time domain gives:

$$\hat{f}_i^{\xi}(t) = T_i^{\xi}\left[\dot{\xi}_i(t) - \int_0^t u_{it}^{\xi}(t) + u_{ic}^{\xi}(t)\,dt\right]. \quad (54)$$

Control command conversion

In the established dual-loop quadrotor control paradigm, the conversion stage maps high-level directives into low-level setpoints. For the zi channel, invoking relation **Eq. 26** furnishes the thrust command $Fiqz$ as:

© 2023 The Author(s). | Published by Agro Intelligence Research Press

$$F_{iqz}^{\mathcal{B}} = \frac{m\left(g - u_i^z\right)}{\cos\,\phi_i\,\cos\,\theta_i}. \qquad (55)$$

Meanwhile, the commands for the xi and yi channels, which encode the desired accelerations, are transformed into the desired roll angle ϕid and pitch angle θid according to:

$$\theta_{id} = \arcsin\left(-\frac{m\left(u_i^x\,\cos\,\psi_i + u_i^y\,\sin\,\psi_i\right)}{F_{iqz}^{\mathcal{B}}\,\cos\,\phi_i}\right), \qquad (56)$$

$$\phi_{id} = \arcsin\left(-\frac{m\left(u_i^x\,\sin\,\psi_i - u_i^y\,\cos\,\psi_i\right)}{F_{iqz}^{\mathcal{B}}}\right). \qquad (57)$$

Singularities that would otherwise occur when:

$$\left|\frac{mu_i^x}{F_{iqz}^{\mathcal{B}}\cos\phi_i\cos\psi_i}\right| > 1 \text{ or } \left|\frac{mu_i^y}{F_{iqz}^{\mathcal{B}}\cos\psi_i}\right| > 1,$$

Are avoided by applying the linear approximation $x \approx \sin{-1}(x)$ to **Eqs. 56 and 57**, which produces the reference signal for the η channel:

$$\eta_{id} = \begin{bmatrix}\theta_{id}\\ \phi_{id}\end{bmatrix} = \begin{bmatrix}-\frac{m\left(u_i^x\cos\psi_i + u_i^y\sin\psi_i\right)}{F_{iqz}^{\mathcal{B}}\cos\phi_i}\\ -\frac{m\left(u_i^x\sin\psi_i - u_i^y\cos\psi_i\right)}{F_{iqz}^{\mathcal{B}}}\end{bmatrix}. \qquad (58)$$

Remark 3. The trajectory-pursuit terms **Eqs. 43 and 45** necessitate the reference signal η˙id and the feedforward signal uidη = η¨id, namely, the first and second temporal derivatives of ηid. In fielded systems where the quadrotors are not expected to execute aggressive maneuvers, these derivative terms become negligible. They can safely be zeroed—a practice adopted by most quadrotor flight control firmware. Should aggressive maneuvering be required, numerical differentiation of ηid may be warranted.

Stability and performance analysis

Singular perturbation theory is applied in this section to examine formation stability and disturbance resilience. The gain requirements that ensure a stable closed loop are collected in the condition below:

© 2023 The Author(s). | Published by Agro Intelligence Research Press

Stability Condition 1. *For the* $\xi \in \{\psi, x, y, z\}$ *channels* $k^{\xi}_{ip} > 0, k^{\xi}_{id} > 0, \alpha^{\xi}_{1} + \alpha^{\xi}_{2} > 0$, *and* $\beta^{\xi}_{1} + \beta^{\xi}_{2} > 0$. *For the* $\eta \in \{\phi, \theta\}$ *channels,* $k^{\eta}_{ip} > 0$, *and* $k^{\eta}_{id} > 0$.

To render parameter tuning more manageable, we introduce the mapping:

$$\begin{cases} T_i^{\xi} = \varepsilon T_i^{\xi *}, & \xi \in \{\psi, x, y, z\}, \\ T_i^{\eta} = \varepsilon T_i^{\eta *}, & \eta \in \{\phi, \theta\}, \end{cases} \quad (59)$$

where ε > 0 emerges as the singular perturbation parameter that couples the UDE settings across the two quadrotors, and $T_i^{\xi} *$ together with $T_i^{\eta} *$ are positive, user-adjustable constants. With these definitions in place, the central analytical results for the proposed guidance and control framework are now presented.

Theorem 1. Suppose Stability Condition 1 is satisfied. Then the following claims are valid:

i. Under the action of the proposed guidance law and UDE-based robust regulators across all six channels, every state of both quadrotors remains bounded;

ii. Both the formation-level trajectory-tracking errors and the inner-loop attitude-angle tracking errors are quantitatively tunable and satisfy.

$$\left|\tilde{\xi}_i(t)\right| \leq \sigma_i^{\xi}(\varepsilon), \quad \forall t > t_i^{\xi}, \quad \xi \in \{\psi, x, y, z\}, \quad (60)$$

$$\left|\tilde{\eta}_i(t)\right| \leq \sigma_i^{\eta}(\varepsilon), \quad \forall t > t_i^{\eta}, \quad \eta \in \{\phi, \theta\}, \quad (61)$$

Where $\sigma_i^{\xi}(\varepsilon)$ *and* $\sigma_i^{\eta}(\varepsilon)$ denote the prescribed ultimate bounds on the tracking residuals $\tilde{\xi}_i(t)$ *and* $\tilde{\eta}_i(t)$, respectively, enjoying the properties ${}_{\sigma i}^{\xi}(\varepsilon) \to 0$ *and* ${}_{\sigma i}^{\eta}(\varepsilon) \to 0$ *as* $_{\varepsilon} \to 0$, *and* t_i^{ξ} *and* t_i^{η} being the respective settling times.

Proof

Remark 4. Claim (ii) of Theorem 1 establishes that tracking fidelity and system robustness are monotonic in ε; that is, by diminishing the solitary parameter ε to amplify the disturbance-rejection potency of the UDE, the quadrotor state tracking deviations can be compressed into an arbitrarily small neighborhood of zero in the steady regime. This characteristic is of considerable practical value, as it makes the tuning procedure for boosting system robustness both elementary and transparent.

Simulation

© 2023 The Author(s). | Published by Agro Intelligence Research Press

Numerical validation of the proposed guidance and control architecture for the dual-quadrotor suspended-payload transport task is conducted in MATLAB/Simulink. The physical parameters of the system, used across all simulation runs, are detailed in **Table 2**, while the corresponding controller gain settings are summarized in **Table 3**.

Table 3. Control gains used in the simulations.

Control channels	Control gains							
	kip	kid	αi	βi	$T*i$	ε	$l1$	$l2$
x	3	2	5	5	1	1	\	\
y	3	2	5	5	1	1	\	\
z	0.5	1	5	5	0.04	1	\	\
ϕ,θ	20	20	\	\	0.05	1	\	\
ψ	3	2	5	5	1	1	100	100

At the start of each trial, the two vehicles occupy the locations $\boldsymbol{P}^{\mathcal{I}}{}_1(0)=[0m,0m,-1m]^T$, $\boldsymbol{P}^{\mathcal{I}}{}_2(0)=[0m,-1m,-1m]^T$, yielding a formation of initial scale $L(0)=1m$ and initial yaw orientation $\delta(0)=0$ rad. Zero initial conditions are imposed on all remaining quantities: attitude angles of the quadrotors, payload oscillation angles, and both translational and rotational rates of the aircraft.

Three separate flight regimes, summarized in **Table 4**, are devised to showcase the framework's proficiency in cooperative lift-off, level forward flight, synchronized turning, in-flight adjustment of inter-vehicle distance, and switching between formation flight modalities. A fourth regime, Scenario 4, is dedicated to examining disturbance resilience against load oscillation; therein, the formation is held in hover while the UDE operates under a set of distinct parameter choices, specifically ε ={0.5, 1, 2, 5}. The detailed outcomes for each regime are presented in the following subsections.

Table 4. Scenarios considered in the simulations.

Scenario No.	Description of the scenario
1	Takeoff and straight-level flight under changing formation dimensions
2	Synchronized circular turning maneuver during flight
3	Obstacle evasion using a dynamically changing flight formation
4	Evaluation of system robustness while maintaining hover flight

Scenario 1

A 10 s stationary hover at the initial positions opens Scenario 1. Following this phase, the pair of aircraft lifts the payload, climbs until reaching the altitude $z_{\mathcal{I}}$=−4 m, and then translates along the $x_{\mathcal{I}}$-axis with a commanded forward speed of 0.1 m/s. During the time window from 40 s to 60 s, the formation scale L undergoes a steady contraction from 1 m down to 0.5 m, after which the tighter spacing is preserved for the remainder of the flight.

The recorded data are plotted in **Figures 6 and 7**. From a stability and robustness perspective, all system states remain bounded throughout the maneuver, and the formation demonstrates resilient trajectory tracking in the presence of oscillatory payload-induced perturbations. A further observation is that the guidance law combined with the cooperative

© 2023 The Author(s). | Published by Agro Intelligence Research Press

controller permits dynamic reconfiguration of the formation scale while a mission is underway—an attribute of clear practical utility in contexts where narrow passages must be traversed, a point reinforced by the results of Scenario 3.

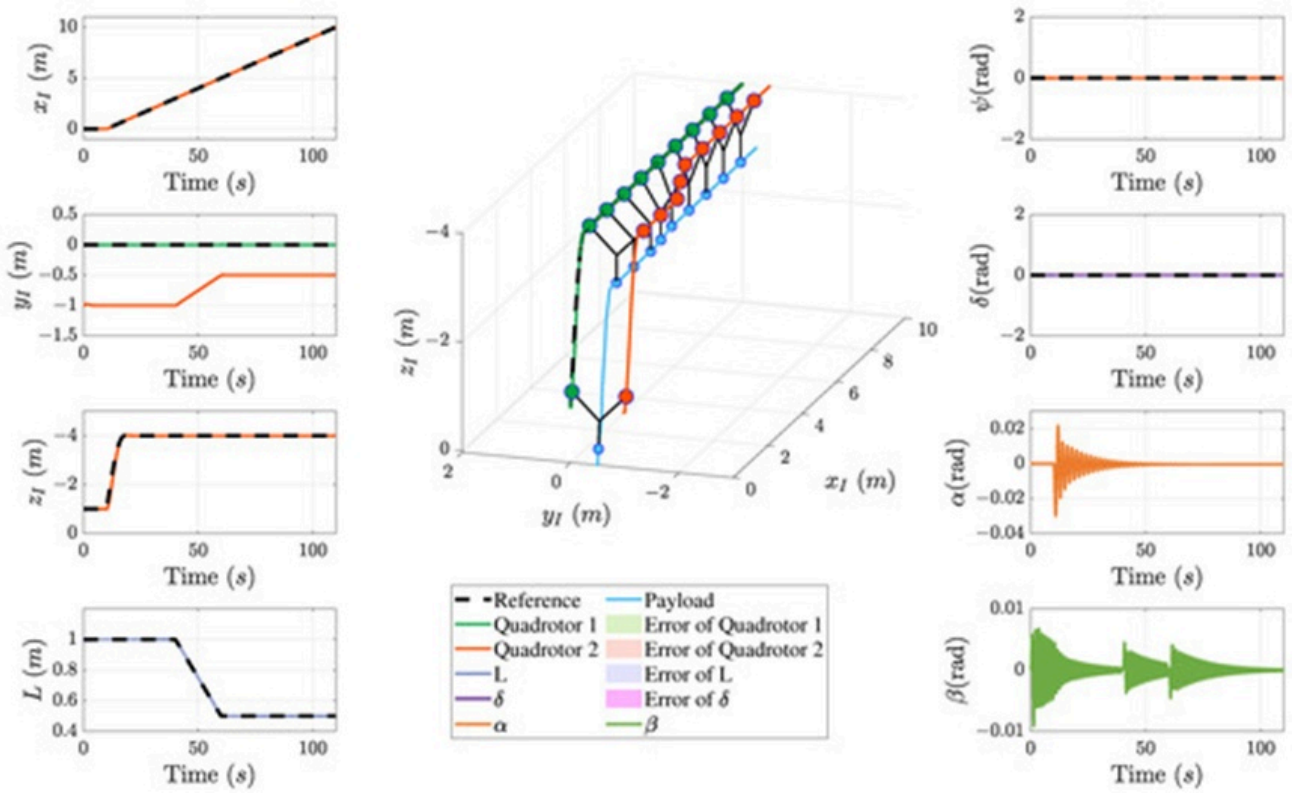

Figure 6. Scenario 1: flight trajectories of the formation and other states of the quadrotors and the payload.

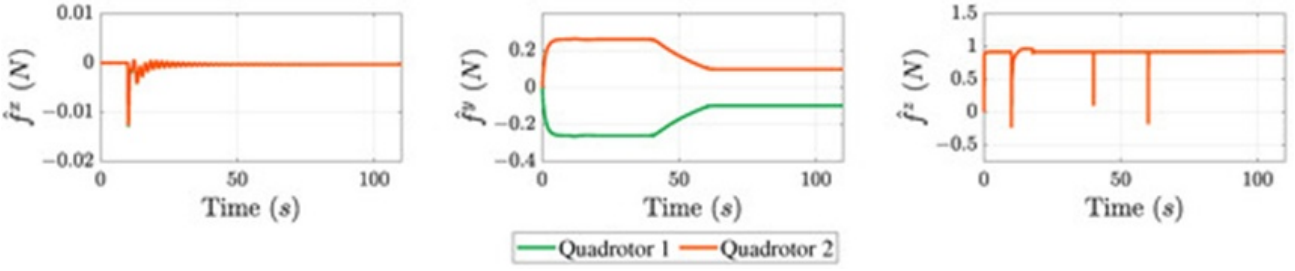

Figure 7. Scenario 1: UDE disturbance estimation signals.

Scenario 2

In contrast to Scenario 1, where forward flight proceeds along the xL1-axis, i.e., perpendicular to the line connecting the two vehicles, Scenario 2 prescribes a lateral translation along the yL1-axis to the waypoint $\boldsymbol{P}_d^l = [0m, 5m, -1m]^T$. Thereafter, a coordinated circular maneuver of radius 5 m is performed by continuously rotating the formation yaw angle δ, the commanded value δd of which increases at a constant rate of 0.1 rad/s.

Figure 8 shows that the lateral movement of the formation excites the payload swing angle β. The UDE, through its disturbance estimation and neutralization action displayed in **Figure 9**, nonetheless ensures that the effect on the formation scale L remains a small transient deviation, as recorded in **Figure 8**. Additionally, high-fidelity, synchronized tracking of the commanded formation yaw angle δd by both quadrotors is achieved throughout the circular path, thereby enabling precise overall trajectory following.

© 2023 The Author(s). | Published by Agro Intelligence Research Press

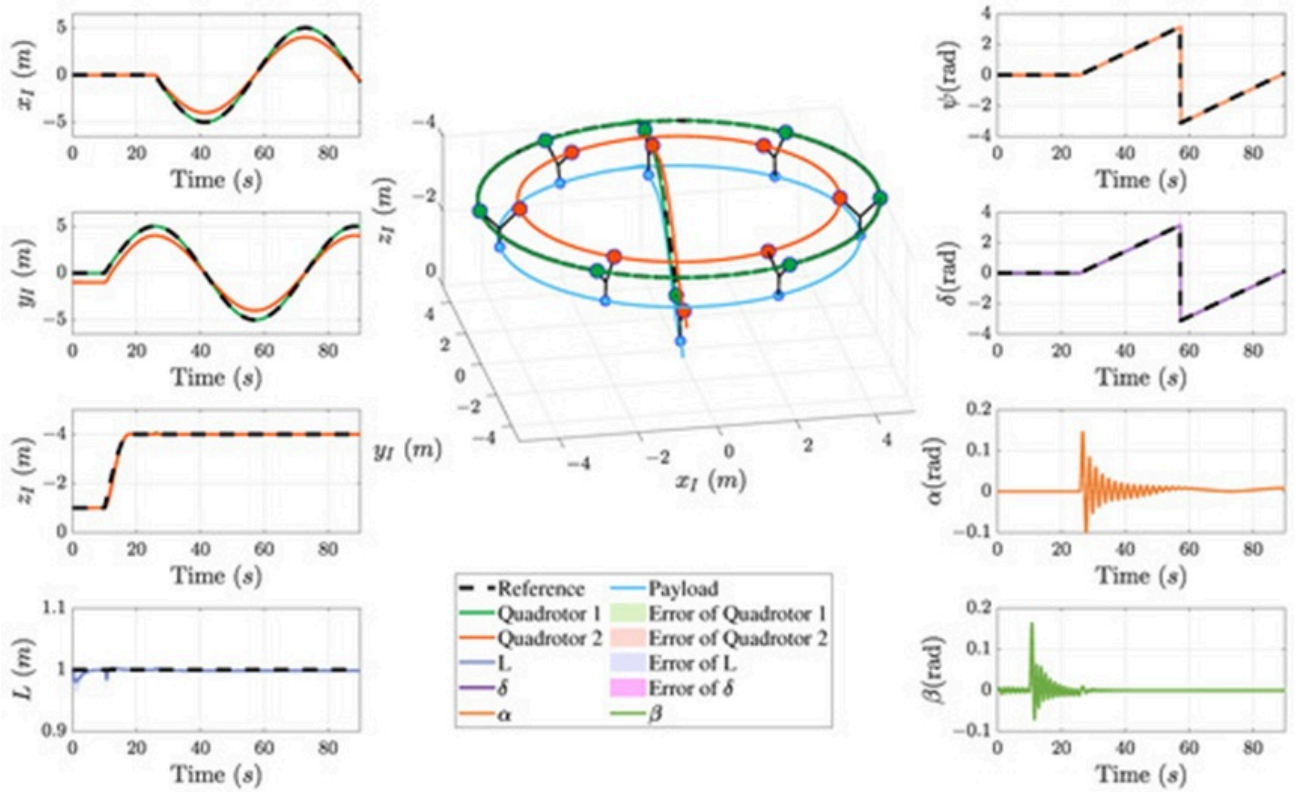

Figure 8. Scenario 2: flight trajectories of the formation and other states of the quadrotors and the payload.

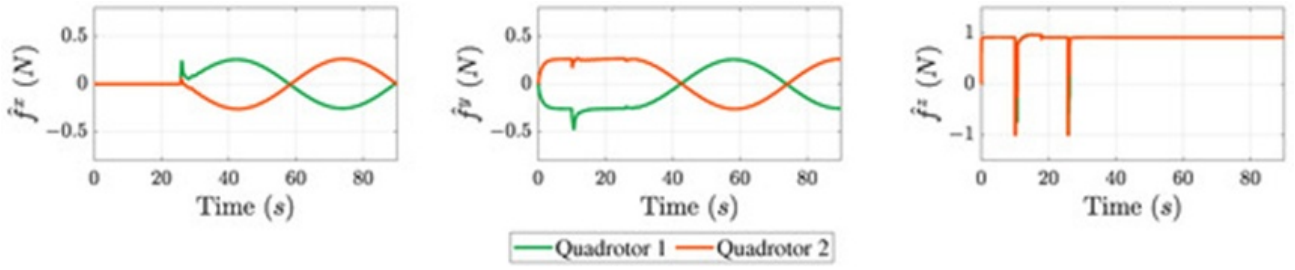

Figure 9. Scenario 2: UDE disturbance estimation signals.

Scenario 3

The strongest illustration of the proposed method's potential is arguably provided by its deployment in a geometrically complex environment, where the quadrotor formation must navigate a confined, winding corridor. **Figures 10 and 11** contain the corresponding simulation outputs. One can observe from **Figure 10** that a reduction in formation scale is triggered during Phase 1 to avert collisions. When, in Phase 2, the passage narrows to a width that prohibits traversal in the standard formation orientation, a switch to lateral flight mode is executed. Once the corridor broadens again in Phase 3, the original inter-vehicle spacing is restored.

© 2023 The Author(s). | Published by Agro Intelligence Research Press

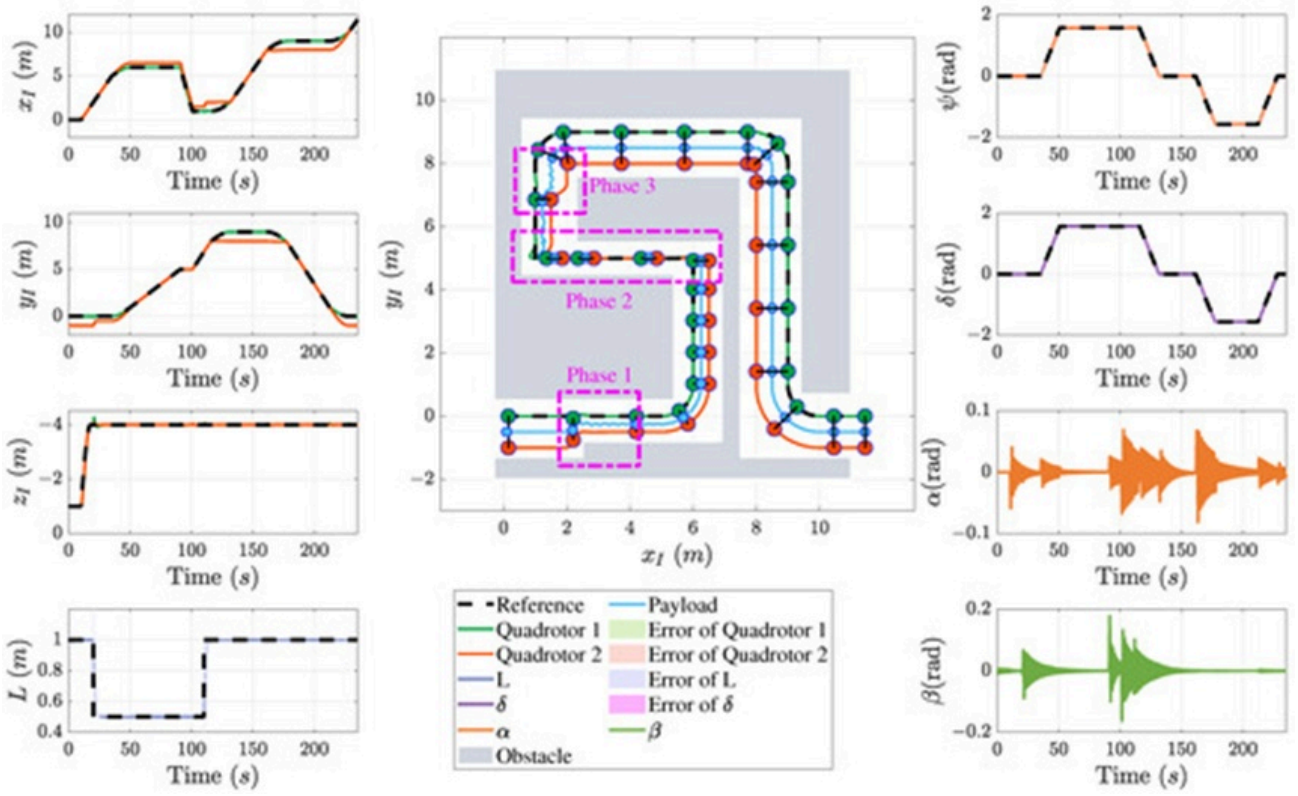

Figure 10. Scenario 3: flight trajectories of the formation and other states of the quadrotors and the payload.

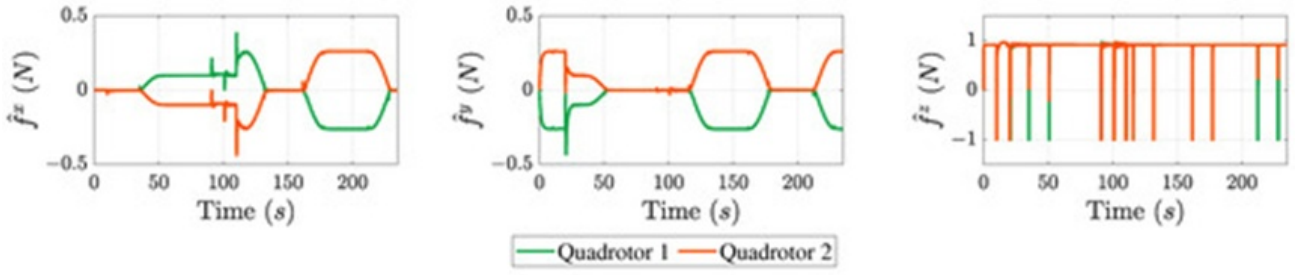

Figure 11. Scenario 3: UDE disturbance estimation signals.

Scenario 4

The purpose of Scenario 4 is to verify the claim made in Theorem 1 of Section 3.5—that making the single parameter ε progressively smaller leads to monotonic improvement in tracking precision. To this end, the UDE is configured with the values ε={0.5,1,2,5}. For a baseline comparison, the controller is also exercised without the UDE active (the case marked "no compensation" in **Figure 12**), thereby isolating the robustness benefit attributable to the UDE. Throughout this scenario, both quadrotors remain in hover at their starting positions. A lateral pulling force component, arising from the payload weight transmitted through the cables, tends to draw the two vehicles together. As **Figure 12** makes evident, feedback regulation unaided by the UDE cannot maintain the formation scale L. By contrast, supplying the UDE with smaller values of ε results in correspondingly tighter regulation of the formation size, i.e., smaller steady-state deviation. This finding is fully in line with statement (ii) of Theorem 1 and highlights the practical tuning advantage embedded in the proposed design.

© 2023 The Author(s). | Published by Agro Intelligence Research Press

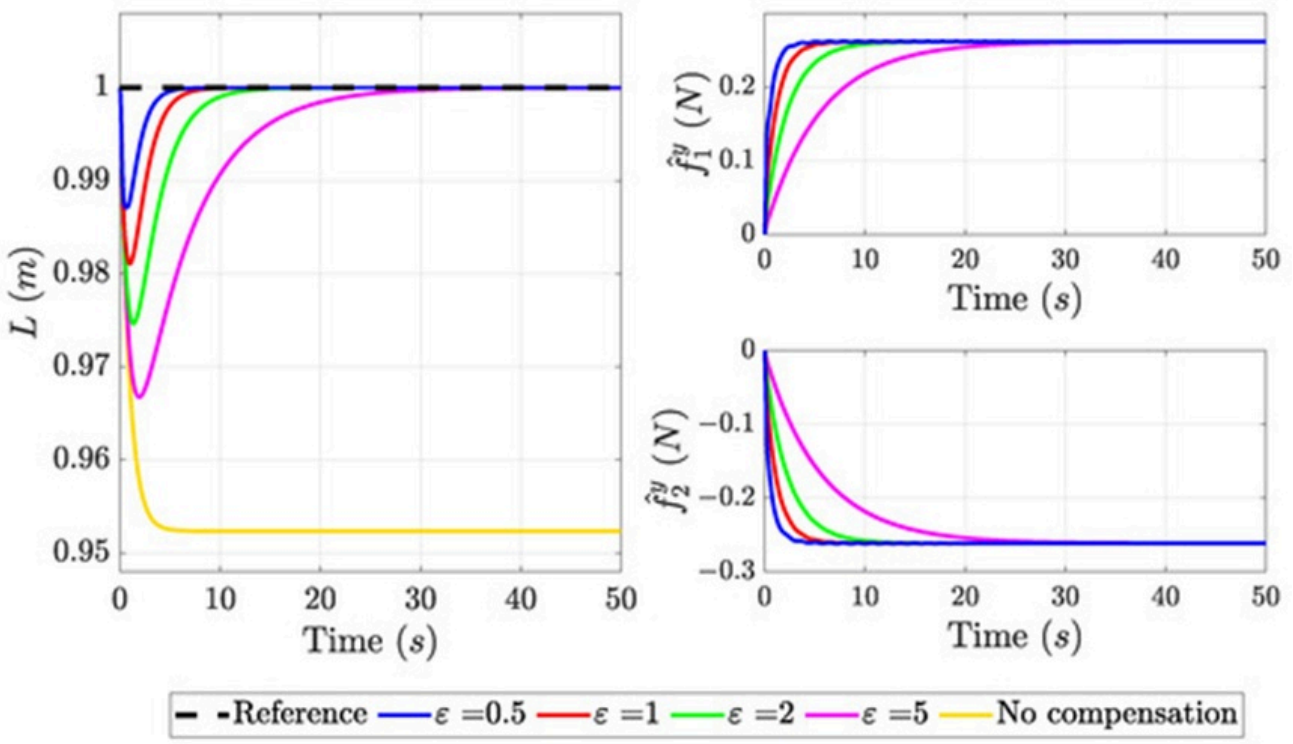

Figure 12. Scenario 4: formation size and UDE disturbance estimation signals under different ε parameters.

Conclusion

This article addresses the guidance and cooperative regulation problem for two quadrotors jointly transporting a cable-suspended load configured in a novel “Y”-shaped geometry. The influence of payload oscillation on the translational behavior of both aircraft is first made explicit by deriving the swing kinematics in terms of quadrotor acceleration and then embedding these kinematics into a comprehensive, nonlinear, mutually coupled dynamical description of the full quadrotor–payload ensemble, whereby the oscillatory motion manifests as perturbing cable tension vectors impressed upon each vehicle. Decoupling of this comprehensive description into six second-order subsystems is accomplished via feedback linearization. The difficulty posed by Quadrotor 2’s lack of direct access to reference trajectories is resolved through a purpose-designed guidance law that synthesizes the missing information from measurable states of Quadrotor 1, supplemented by estimates of unmeasurable state derivatives obtained from a Luenberger state observer. A cooperative regulator, augmented with an uncertainty and disturbance estimator that actively neutralizes payload-induced oscillations, is then constructed atop the local reference signals provided by the guidance law and the inter-vehicle state exchange, thereby securing robust trajectory tracking in a commanded, possibly time-varying formation. Singular perturbation theory underpins a performance investigation that reveals a practically compelling feature: the capacity to simultaneously sharpen disturbance attenuation and overall tracking accuracy by adjusting a single parameter, ε. Results from numerical simulations covering three representative scenarios confirm both the effectiveness of the proposed methodology and its capability to accomplish obstacle avoidance via real-time adaptation of formation scale and flight modality.

About future extensions, the ambition is to broaden the reach of the proposed technique to cooperative formation control involving multiple quadrotors that collectively suspend a payload via cables arranged in a “Y”-like topology. The envisaged concrete developments include (1) formulating a generic model for such multi-agent payload transport systems and (2) devising a cooperative guidance law and distributed local robust controllers employing tools from multi-agent distributed control theory.

© 2023 The Author(s). | Published by Agro Intelligence Research Press

Abbreviations

The following abbreviations are used in this manuscript:

UDE	uncertainty and disturbance estimator
LSO	Luenberger state observer

Acknowledgements

None

Conflict of interest

None

Financial support

This research was funded in part by the Sichuan Science and Technology Program (Natural Science Foundation of Sichuan Province) under Grant No. 2023NSFSC1430 and by the Fundamental Research Funds for the Central Universities under Grant No. 2682023CX082.

Ethics statement

None

Received: 11 Aug 2022 Revised: 16 Oct 2022 Accepted: 02 Nov 2022
Published online: 25 November 2023

Rights and permissions

Open Access The author(s) retain copyright. This article is licensed under the Creative Commons Attribution-NonCommercial-ShareAlike 4.0 International License. It may be shared and adapted for non-commercial purposes with appropriate attribution, an indication of changes, and distribution of adaptations under the same license. Third-party material may be subject to separate terms identified in its credit line. View the license at https://creativecommons.org/licenses/by-nc-sa/4.0/.

References

1. Liang X, Fang YC, Sun N, Lin H. Nonlinear hierarchical control for unmanned quadrotor transportation systems. IEEE Trans Ind Electron. 2017;65:3395-405.

2. Qian LH, Graham S, Liu HHT. Guidance and control law design for a slung payload in autonomous landing: A drone delivery case study. IEEE ASME Trans Mechatronics. 2020;25:1773-82.

3. Yang S, Xian B. Energy-based nonlinear adaptive control design for the quadrotor uav system with a suspended payload. IEEE Trans Ind Electron. 2019;67:2054-64.

4. Gimenez J, Gandolfo DC, Salinas LR, Rosales C, Carelli R. Multi-objective control for cooperative payload transport with rotorcraft uavs. ISA Trans. 2018;80:491-502.

5. Liang X, Zhang Z, Yu H, Wang Y, Fang YC, Han JD. Antiswing control for aerial transportation of the suspended cargo by dual quadrotor uavs. IEEE ASME Trans Mechatronics. 2022;27:5159-72.

6. Alothman Y, Guo MH, Gu DB. using iterative lqr to control two quadrotors transporting a cable-suspended load. IFAC-PapersOnLine. 2017;50:4324-9.

7. Villa DKD, Brandão AS, Carelli R, Sarcinelli-Filho M. Cooperative load transportation with two quadrotors using adaptive control. IEEE Access. 2021;9:129148-60.

8. Pereira PO, Dimarogonas DV. Nonlinear Pose Tracking Controller for Bar Tethered to Two Aerial Vehicles with Bounded Linear and Angular Accelerations. In: Proceedings of the 2017 IEEE 56th Annual Conference on Decision and Control (CDC), Melbourne, Australia; 2017. p. 4260-5.

9. Prajapati P, Parekh S, Vashista V. Collaborative Transportation of Cable-Suspended Payload using Two Quadcopters with Human in the loop. In: Proceedings of the 2019 28th IEEE International Conference on Robot and Human Interactive Communication (RO-MAN), New Delhi, India; 2019. p. 1-6.

10. Ccari LFC, Yanyachi PR. A novel neural network-based robust adaptive formation control for cooperative transport of a payload using two underactuated quadcopters. IEEE Access. 2023;11:36015-28.

11. Aliyu A, El Ferik S. Control of multiple-uav conveying slung load with obstacle avoidance. IEEE Access. 2022;10:62247-57.

12. Chen T, Shan JJ. Cooperative Transportation of Cable-suspended Slender Payload Using Two Quadrotors. In: Proceedings of the 2019 IEEE International Conference on Unmanned Systems (ICUS), Beijing, China; 2019. p. 432-7.

13. Tang S, Sreenath K, Kumar V. Aggressive Maneuvering of a Quadrotor with a Cable-Suspended Payload. In: Proceedings of the Robotics: Science and Systems, Workshop on Women in Robotics, Berkeley, CA, USA; 2014. p. 1-20.

14. Chai Y, Liang X, Yang ZC, Han JD. Energy-based nonlinear adaptive control for collaborative transportation systems. Aerosp Sci Technol. 2022;126:107510.

15. Lin DS, Han JD, Li K, Zhang JL, Zhang CY. Payload transporting with two quadrotors by centralized reinforcement learning method. IEEE Trans Aerosp Electron Syst. 2023;60:239-51.

16. Lu Q, Ren BB, Parameswaran S. Uncertainty and disturbance estimator-based global trajectory tracking control for a quadrotor. IEEE ASME Trans Mechatronics. 2020;25:1519-30.

17. Zhong QC, Rees D. Control of uncertain lti systems based on an uncertainty and disturbance estimator. J Dyn Sys Meas Control. 2004;126:905-10.

18. Khalil HK, Grizzle JW. Nonlinear Systems, 3rd ed. Prentice-Hall: Upper Saddle River, NJ, USA; 2002. p. 176-7.

© 2023 The Author(s). | Published by Agro Intelligence Research Press